Investigating the Petrology and Microstructures of Achondrite Meteorites

Faye Davies

Submitted in fulfilment of the requirements for the Degree of Master of Research (Earth Science)

School of Engineering
College of Science and Engineering
University of Glasgow

April 2023

Abstract

Achondrite meteorites provide us with important information about differentiated planetary bodies of the early Solar System, as these meteorites have been melted and recrystallised to various degrees throughout their geological history with the source of these meteorites being the outer shell of differentiated parent bodies. The textural relationships within achondrite meteorites provide important evidence of the formation, size, evolution and destruction of the Solar System's first planetesimals.

The focus of this research is using a variety of achondrite meteorites similar to rocks which are found on Earth. Using a range of SEM techniques such as EDS, EBSD and EMPA to observe the crystallography of each meteorite and study the deformation structures and relationship between the grains to provide an insight into the history of the planetary bodies from which each of these meteorites originated.

The key findings from this research were that ureilites have olivine grains that display Mg-rich reduction rims with Fe-metal blebs surrounding Mg-poor cores as well as iron veining throughout the samples. These textures are interpreted as a redox reaction where carbon acts as a catalyst reacting with Fe within the olivine grains forming Mg-rich rims and Fe-metal veining throughout the samples. The degree to which the reaction has taken place varies between the samples based on the carbon and iron percentages observed as a decrease in carbon percentage resulting in an increase in the iron percentage of the sample for each ureilite studied within the research. Anomalous achondrite MIL 090356 displays similar chemical reactions to the ureilites and these are interpreted to be caused by an impact event on the parent body. While iron veining is still present on MIL 090356, the catalyst for the reaction is sulphur infiltration within the sample rather than carbon as was the case for the ureilites. Evidence for similar Sulphur catalysed chemical reactions have also been suggested for brachinites which MIL 090356 is closely affiliated. This provides evidence that similar chemical processes occurred on more than one planetary body beyond 1 AU from the Sun within the same outer region of the solar nebula. The aubrite Cumberland Falls which formed within the inner 1 AU of the early Solar System contains chondritic material including barred olivine-pyroxene chondrules, this chondritic material is classified as enstatite chondrite. These enstatite clasts have not been found before and add to the suite of ordinary chondrite clasts and forsterite chondrite clasts that have been described previously.

Together these chondritic clasts provide evidence of complete mixing of chondritic material within the inner Solar System.

This research has provided an insight into processes of other planetary bodies and their formation as well as the earliest periods in the solar system history allowing for a more in-depth complete picture of the behaviour of rocky worlds in the solar system.

Table of Contents

Contents of Tables

Contents of Figures

Acknowledgements

Firstly, I would like to thank my supervisor Dr Luke Daly for the opportunity to complete this master's as well as all the support offered as my supervisor during the time, I have taken to complete my master's as well as Dr Lydia Hallis my second supervisor for all her support and read-throughs of my final thesis.

I would like to thank the Smithsonian Museum in Washington D.C for the loan of the samples, which without this project would not be possible along with the technicians at the University of Glasgow for getting the SEM up and running and keeping it working throughout my studies as well as the help and supported offered during my data collection.

Also, like to thank my family for their reliable support when applying for this master's and throughout the thesis itself supporting each choice I made as well as my friends for all their support and ensuring that I take time off to laugh, have fun and most of all enjoy the beautiful outdoors of Scotland which I have loved greatly during my time living in Scotland.

Finally, I would like to thank those in the PhD community at the University of Glasgow who welcomed me into their community as a PGR student making Glasgow feel like home during COVID, along with those in the PhD Society whom I had the pleasure to be their president even though I was still a masters student and all those in the PGR office at the Molema building helping to keep me sane, feel part of the community, provide plenty of laughs and offer their support when it was needed most.

Authors declaration

I declare that this thesis, except where acknowledgement to others is given, represents my own work carried out in the School of Geographical and Earth Sciences, University of Glasgow. The research presented here has not been submitted for any other degree at the University of Glasgow, or at any other institution. Any published or unpublished work by other authors has been given full acknowledgement in the text.

Abbreviations

Al ……	Aluminium
ANSMET ……	Antarctic Search for Meteorites
AU ……..	Astronomical Unit
BSE …….	Backscatter Electron
ºC ……	Celsius
C ……..	Carbon
Ca ……	Calcium
CC ……...	Carbonaceous Chondrites
CCAM ……	Carbonaceous chondrite Anhydrous Mineral
CH_4 …….	Methane formula
Cl ……	Chlorite
CO ……...	Ornans-like Carbonaceous Chondrite
$CO_{(g)}$ ……	Carbon Monxide formula (gaseous form)
Cr ……	Chromium
CRA ……	Crystal Rotation Axis
CV ……...	Vigarano-like Carbonaceous chondrites
E ……..	Enstatite
EBSD ……..	Electron Backscatter Data
EDS …….	Energy Dispersive Spectroscopy
EH ……...	Enstatite High
EL ……...	Enstatite Low
EMPA …….	Electron Microprobe Analysis
Fe ……	Iron
$FeMgSiO_4$ ……...	Magnesium Iron Silicate Formula (Olivine)
Fo ……	Forsterite
g ……..	Grams
Ga ……	Billions of years
gcm^{-3} ……...	gram/centimetre
GOS ……	Grain Orientation Spread
Gpa …….	GigaPascals
GROD …….	Grain Relative Orientation Distribution
H_2O …….	Water formula
HED ……	Howardites Eucrites Diogenites

ISAAC ……	Imaging Spectroscopy and Analysis Centre
K ……	Kelvin
KAM ……...	Kernel Average Misorientation
keV ……..	Kiloelectron Volts
Km ……..	Kilometer
kV ……...	Kilovolt
LL ……...	Low iron-low metal Ordinary Chondrite
m …….	Meter
Ma ……...	Millions of years
Mg# …….	Magnesium Number
Mg ……...	Magnesium
$MgSiO_3$ ……...	Magnesium Silicate Formula (Pyroxene)
MIL …….	Miller Range Mountains
Mm ……..	Millimetre
Mn ……...	Manganese
MOS ……	Mean Orientation Spread
Mpa …….	Megapascals
Na ……	Sodium
na ……...	Nanoamps
Nd ……...	Neodymium
Ni ……	Nickel
nm ……..	Nanometres
O …….	Oxygen
OC ……...	Ordinary Chondrite
P ……..	Phosphorous
Pa ……	Pascals
pdf ……...	Planar Deformation Features
Pb ……	Lead
REE …….	Rare Earth Elements
S ……..	Sulphur
SE ……	Secondary Electron
SEM ……	Scanning Electron Microscope
Si …….	Silicon
Sm ……...	Samarium
SNC ……	Shergottites-Naktilites-Chassignite group

TFL …….	Terrestrial Fractionation Line
Ti …….	Titanium
U …….	Uranium
UPB ……	Ureilite Parent Body
wt% …….	Weight percent
XCT ……	X-ray computed tomography
µm ……...	Micrometre
µa ……	Microampere

1. Introduction

1.1 Introduction to the Project

The question which shall be addressed throughout this thesis is how the microstructure and textures of achondrite meteorites can vary between subgroups, thus providing a deeper understanding of the planetary body processes in different regions of the Solar System from which they originated. The microstructure and petrology of three achondrite types, aubrites, ureilites and an anomalous achondrite will be analysed by scanning electron microscopy (SEM), energy dispersive X-Ray spectroscopy (EDS) and electron backscatter diffraction (EBSD) to determine the processes that occurred on the parent bodies of each meteorite group, assess the similarities and/or differences between each individual meteorite and the different achondrite groups being studied in this project.

Achondrite meteorites are samples from the mantle and crust of differentiated planetary bodies of the early Solar System, they are predominantly igneous rocks and therefore, preserve evidence of the igneous processes that occurred on their parent planetesimal (McSween, 1987). The term planetesimals has been defined by Raymond et al. (2009) as large bodies that are between 100 m – 100 km in size. Igneous processes allow the planetesimal to differentiate from a homogeneous body to one with a compositionally distinct core, mantle, and crust. The process of a global magma ocean melting is driven by heat generated by the decay of short-lived nuclides for smaller planetesimals with larger bodies like the Earth also using additional heat generated by accretionary impacts to drive further melting (Schaefer and Elkins-Tanton, 2018). The formation of a magma ocean facilitates the differentiation process.

To understand the petrology and microstructures of achondrite meteorites a variety of achondrites will be studied using SEM-based techniques including EDS and EBSD. The methodology for this study is to use EBSD and EDS data to analyse and study the deformation, textures, and mineral relationships of crystals within the ureilite meteorite samples Reid 016, Nova 001 and Haverö, the aubrite Cumberland Falls and an ungrouped achondrite sample MIL 090356.

The findings of this project will allow for a greater understanding of the geological processes that occurred on these meteorite’s parent planetesimal. This will provide a better

understanding of how the parent bodies of these meteorites were disrupted and the processes which occurred on them prior to and during their disruption destruction. The purpose of this investigation is to provide an insight into the variability between and within three meteorite groups of planetary bodies which once existed in the Solar System and the processes that acted on them.

1.2 Meteorite Classification and Significance

Meteorites offer a unique source for information about the earliest history of the Solar System, as fragments of extra-terrestrial rock which have landed on Earth and are largely derived from asteroids (Cumming,1969). However, the meteorites discovered on Earth provide an incomplete sample set of the asteroids within the asteroid belt (Grady and Wright, 2006). These are the remains of the first planetesimals that formed in the protoplanetary disk and are in the solar orbit between Mars and Jupiter (Bevan, 2007). These remain unchanged since their formation 4.55 billion years (Ga) ago (Bevan, 2007). Some rare types of carbonaceous meteorites hold water and complex carbon compounds, including amino acids (Rollinson, 2009). Thus, meteorites can provide direct information on the earliest stages of planet formation in the solar nebula during which, gas and dust began to rotate around a young sun. In addition, these meteorites and their parent bodies provide an important record of the conditions that were present and the processes that operated during planetary accretion, formation, differentiation, and evolution (Weisberg et al., 2006; Ciesla et al., 2013). Therefore, information on these processes can be obtained by studying meteorites as remnants of planetesimals found in the asteroid belt (Johansen et al., 2015).

The original planetesimal sources for the rocks present in asteroids and meteorites have for the most part been destroyed during collisions between planetesimals that resulted in the disruption of these early planetesimals (Chambers and Wetherill, 2001). Leftover planetesimals from planet formation are found in the form of asteroids, trans-Neptunian objects and comets which provide a unique record of the physical conditions in the solar nebula. Most planetesimals have been accreted into planets, collided with the sun or were destroyed in giant impacts with other planets (Johansen et al., 2015).

Most extra-terrestrial material comes from the asteroid belt which has lost >99.9% of its solid mass since the planets formed (Grady and Wright, 2006). Models for the protoplanetary

nebula suggest it was around 2-4 astronomical units (AU) from the Sun (Grady and Wright, 2006). Over time the orbits of asteroids can be changed due to a combination of gravitational, collisional and thermal radiation effects which could cause them to leave the asteroid belt and drift towards Earth (Chambers and Wetherill, 2001).

The classification of meteorites is largely based on their mineralogical and petrological characteristics as well as the whole rock chemical and O-isotopic compositions (Fig.1; Weisberg et al., 2006).

Meteorites are categorised into three main groups: iron, stony and stony-iron. Iron meteorites consist of nickel-iron alloys representing the core of the asteroids and other planetary bodies providing information on the metallic cores of planets. Stony meteorites (the most common type of meteorite group) are composed mostly of silicate minerals although many also contain small metal grains and are split into two groups chondrite (oldest material in the Solar System) and achondrite (melt from differentiated rocky planets) with further subgroups being defined based on the meteorites petrology and isotope geochemistry.

Among stony meteorites, the ordinary chondrites group makes up 90.3%, other chondrites 5.8% and stony achondrites 3.9% (Rochette et al., 2009). Chondrite meteorites are a kind of cosmic sediment, an accretion of the first solid materials that formed in the early Solar System within the first few million years of Solar System history, having experienced little if any chemical or physical change since their formation and remaining undifferentiated. These stony meteorites provide insights into the formation of rocky planets in the Solar System which are made up of metals and silicates, offering an insight into the conditions of the planetary body (McSween, 1987). Meanwhile, achondrites make-up around 8% of modern meteorite Falls and typically have textures suggesting that they formed in similar ways to some igneous and volcanic rocks on Earth, with some impact breccias, however, most achondrites are asteroidal in origin (Bevan, 1996).

The broad characteristics used to describe meteorites can be further classified as either undifferentiated or differentiated. Undifferentiated meteorites such as chondrites are fragments from the parent bodies that have not undergone melting and differentiation and therefore contain pristine samples of early Solar System material. This is due to the minerals forming largely in the protoplanetary disk and being accreted in planetary bodies that were not large enough to melt and differentiate. Whereas differentiated meteorites which include

iron, stony-irons and the achondrites are the fragments from parent bodies which underwent planetesimal scale melting and differentiation which formed a core, mantle and crust, with achondrites being the upper mantle/crust of these planetary bodies (Johansen et al., 2015).

Achondrite meteorites are igneous rocks (melts, partial melts and melt residues) or breccias of igneous rock fragments from differentiated asteroids (e.g., Vesta), the Moon and planetary bodies (e.g., Mars) (McSween, 1987). Some achondrite meteorites are impactites, however, achondrites are predominantly igneous rocks and the product of partial melting and crystallisation processes in the upper mantle or crust of differentiated planetesimals (McSween, 1987). There are two types of achondrites: primitive which are residues from partial melting and asteroidal achondrites which form from the crystallisation of magma. It is believed that chondrites are the precursor material to achondrites. (McSween, 1999).

Planetary achondrites include Lunar meteorites, which are likely to have been ejected from the Moon in low-angle large impacts and have affinities to Lunar rocks collected during the Apollo space missions (Bevan, 1996). Lunar meteorites are predominantly classified by their texture petrology and chemistry which hold a wide range of rock types including brecciated and unbrecciated mare basalts, mixed mare/highland breccias, highland regolith breccias and highland impact melt breccias, along with having common chemical signatures such as Fe/Mn ratios in pyroxenes, bulk chemistry, and O-isotopic compositions (Weisberg et al., 2006). Martian meteorites also fall into the planetary achondrite classification of meteorites and have been linked to Mars by comparing trapped gasses in impact melts in the meteorite with measurements of the Martian atmosphere collected by the Viking lander. There are three main groups of Martian meteorites collectively called SNC (shergottites-nakhlites-chassignite group) that all have igneous textures.

Primitive achondrites have an achondritic texture but have retained a primitive chondrite-like chemical signature (Weisberg et al., 2006). For example, in ureilites (classification of primitive achondrite), O isotopes are heterogeneous and plot on the CCAM (Carbonaceous Chondrite Anhydrous Mineral) line rather than the TFL (Terrestrial Fractionation Line) (Weisberg et al., 2006). This implies that the oxygen isotope signature is of a primitive Solar System material as opposed to chemically fractionated material (Goodrich, 1992). Primitive achondrites are generally thought to form from chondrites, that exceeded their solidus temperature on their parent body and thus experienced partial melting or crystallised from

melts on a parent body on which planetary differentiation did not achieve isotopic equilibrium (Weisberg et al., 2006).

The characteristics of primitive achondrites are planetary-type noble gas compositions, heterogenous O isotopes and high concentrations of trace siderophile elements along with evolved igneous textures, fabrics and mineralogy, low concentrations of volatile elements, fractionated rare Earth element (REE) (group of chemically similar metal elements) patterns and high Ca/Al ratios (Rubin, 2006).

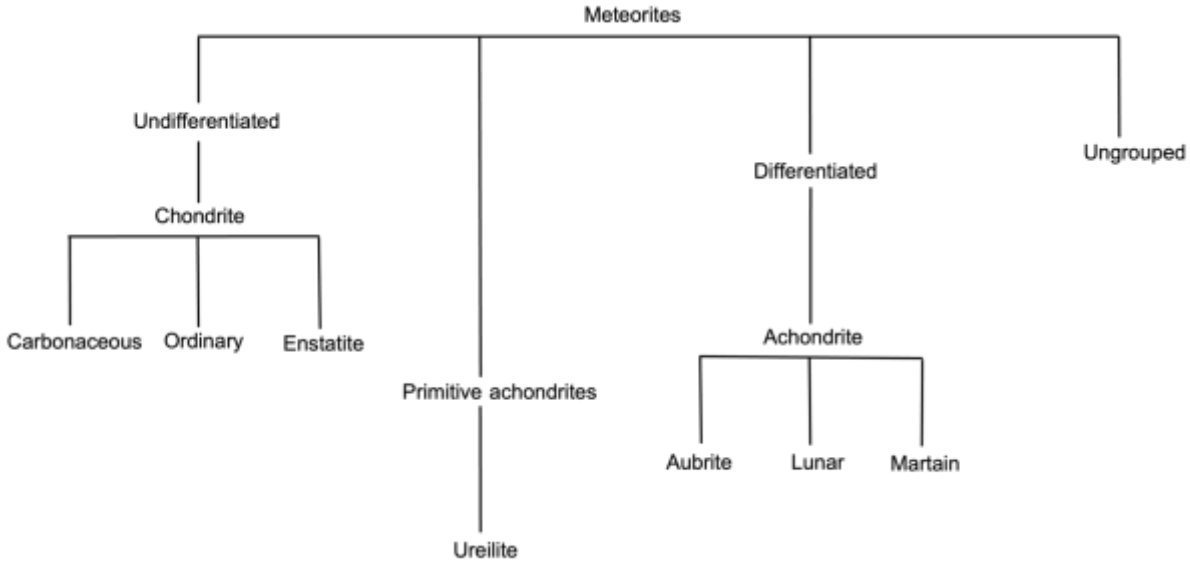

Figure 1: Simplified schematic of meteorite classification tree based on the Prior (1920) and Mason (1967) classification showing the major meteorite divisions, with a focus on the meteorites which this project is focusing on; primitive achondrite (ureilite), the achondrite (aubrite) and an ungrouped meteorite (Adaptation from Weisberg et al., 2006).

1.3 Meteorite Shock Classification

Shock metamorphism is a key characteristic of impact events caused by interplanetary collisions of the Solar System between all terrestrial bodies (Stöffler et al., 2018). Natural shock metamorphism is caused through high-impact collisions of planetary material with another solid rock target, producing shock waves whose heat and pressure alter and sometimes melt the surrounding rock, forming shock metamorphism textures (Stöffler et al., 2018). These textures can provide information into the peak shock pressures, shock wave

direction and propagation and the impact itself based on shock metamorphism classification (Stöffler et al., 2018).

Shock metamorphism and brecciation resulting from hypervelocity collisions on their parent bodies are one of the most common features within meteorites (Stöffler et al., 1991). Meteorites are classified in terms of the nature and intensity of shock-derived microstructures into six shock stages which are broadly defined by optical petrographic investigations of the microstructural shock effects of olivine and plagioclase in petrographic thin section as classified in Table 1 a revised version of the table produced by Stöffler et al., 2018.

Different shock pressures produce a variety of distinctive shock microstructures thus observation of calibrated shock microstructures can be used to both classify the meteorites shock stage and peak shock pressure. The current shock classification system has been defined for eight rock and sediment classes assigned into three major groups: (1) crystalline rocks (2) chondritic rocks and (3) sedimentary rocks and sediments. (Bevan, 2007; Stöffler et al., 2018).

Table 1: Shock classification of achondrite meteorites including the seven shock stages petrographic observations, approximate shock pressures and post-shock temperatures for meteorite samples, adapted from (Stöffler et al., 2018)

Shock Stage	Shock effects	Equilibration Shock Pressure (Gpa)	Post Shock Temperature (°C)
(S1) Stage 1	Sharp optical extinction of all minerals, Irregular fracturing		
(S2) Stage 2	Fractured silicate, mechanical twinning of pyroxene, kink bands in mica	~1-5	~0
(S3) Stage 3	Plagioclase with planar deformation features (pdf) and partially converted to diaplectic glass, mosaicism in plagioclase and mafic minerals, pf in olivine	~20-22	~50-150
(S4) Stage 4	Diaplectic plagioclase glass, mechanical twinning in pyroxene, mosaicism in mafic minerals, pf in olivine	~28-34	~200-250
(S5) Stage 5	Melted plagioclase glass with incipient flow structure and vesicles, mosaicism in mafics minerals, pdf in pyroxene and amphibole, loss of pleochroism in mafic minerals	~42-45	~900
(S6) Stage 6	Melted plagioclase glass with vesicles and flow structure, incipient and increasing contact melting of pyroxene and olivine and (re)crystallisation of olivine	~55-60	~1100
(S7) Stage 7	Whole rock melt	>~60-65	~1500

1.4 Terrestrial Weathering

Depending on if a meteorite sample is a find or fall it is important to note the amount of time at which the sample has been exposed to the Earth's atmosphere and environment (Weisberg et al., 2006). The effects of the Earth's environment on meteorites are a change in the chemistry and structures within the samples depending on the time exposed altering and effecting the information that can be gained as well as the accuracy of this information collected from each individual sample, therefore quick sample recovery is of high importance.

Meteorites which were observed entering Earth's atmosphere as a fireball and were subsequently recovered are classed as falls. In contrast, meteorites that have been fortuitously recovered in the absence of an observed fireball event are classed as finds (Weisberg et al., 2006). This distinction between fall and find is important because the time the meteorite then spends on Earth can affect the composition and mineralogy of the rock due to terrestrial weathering (Weisberg et al., 2006).

The weathering of meteorites is classified as the alteration of the original component phases within the meteorite to phases which are more stable at the Earth's surface, upon entering the Earth's atmosphere when the interaction with the terrestrial environment begins (Bland et al., 2006). The most affected part of meteorites chemistry from terrestrial weathering is the metals present becoming oxidised, silicates also being altered, with phyllosilicates forming locally on olivine and then more massively in all mafic silicates (Jull et al., 1991).

There are various weathering scales for meteorites, based on both hot and cold desert climates focusing on carbonaceous and ordinary chondrites more, however, the classifications can also be used for irons and achondrites (Bland et al., 2006). The following scales of weathering are currently in use at the NASA Johnson Space Centre in Houston, adopting the following weathering scale for hand specimens which is as follows; A (minor rustiness) B (moderate rustiness) and C (severe rustiness), with a similar scale for degrees of fracturing (Bland et al., 2006). The weathering scale for polished thin sections has been adapted from Wlotzka (1993) (Table 2), this scale follows a six-category system which begins with minor weathering of metals then troilite, through to silicates, with the differences between hot and cold desert climates being that the weathering takes a longer period of time compared to that of meteorites found in hotter climates.

Table 2: Weathering scale classification of polished thin section meteorites including the weathering stage and classification features of each category identified with such stage adapted from (Wlotzka, 1993).

Weathering Stage (Category)	Category features
W0	No visible oxidation of metal or sulphides. A limonitic staining may already be noticeable in transmitting light. Fresh falls are usually of this grade although some are already W1.
W1	Minor oxide rims around metal and troilite, minor oxide veins.
W2	Moderate oxidisation of metal, about 20-60% being affected.
W3	Heavy oxidation of metal and troilite 60-95% being replaced.
W4	Complete (>95%) oxidisation of metal and troilite, but no alteration of silicates.
W5	Beginning alteration of mafic silicates, mainly along cracks.
W6	Massive replacement of silicates by clay minerals and oxides.

1.5 Introduction of Meteorites

1.5.1 Ureilite Meteorites

The first meteorite group studied as part of this thesis is the ureilite group, which are primitive achondrites and the second largest group of achondrite meteorites. However, there are no good candidates in the asteroid belt for the ureilite parent body yet identified (Goodrich et al., 1987). The first ureilite (Novo Urei) was found in September 1886 when

several pieces were discovered near the village of Novo Urei, Krasnoslobodsk district in Russia (McSween, 1987).

The ureilites mineralogy consists primarily of coarse-grained (mm sized) olivine and pyroxene crystals with grain boundaries at 120º triple junctions indicating a high degree of textural equilibrium, with some showing evidence of cumulate origin and textures (Downes et al., 2008). Filling the spaces between the larger silicate grains is a carbon-rich matrix of graphite and/or diamond, iron-nickel metal, troilite or other minor phases (Downes et al., 2008; McSween, 1987). Ureilites are plutonic rocks, but it is disputed as to whether they formed from accumulations of minerals in a magma chamber or are residual crystals leftover from a partial melting (McSween, 1987; Rubin, 2006). Early theories of ureilite petrogenesis were that they formed as igneous cumulates however the discovery of enormous oxygen isotopic diversity within ureilites caused an abrupt shift in ureilite petrogenetic theory, as correlations showed that the processes formed through the solar nebula and not igneous processes of the parent bodies (Warren et al., 2006). The oxygen isotope data, alongside high abundances of highly siderophile elements, indicates that their origin as the remains of an asteroidal mantle are more likely than cumulate origin (Warren et al., 2006).

There are three major types of ureilites (1) olivine-pigeonite (2) olivine-orthopyroxene and (3) polymict ureilites (Weisberg et al., 2006). Most ureilites tend to be devoid of feldspar with the exception being the polymict ureilites and other rare exceptions (Weisberg et al., 2006).

Most ureilites are monomict (formed of one rock type) breccias with some being polymict (formed of multiple rock types) breccias. Polymict ureilites have been interpreted as sampling near surface material of ureilite parent asteroid, this was inferred from the presence of implantation of solar wind gases found in them (Downes et al., 2008). However, a study of >500 olivine and pyroxene clasts found within several ureilites revealed a statistically identical range of compositions in ureilite polymict breccias, to those in the unbrecciated ureilites suggesting they originated from the same parent asteroid (Downes et al., 2008).

The ultramafic petrology of this meteorite, along with the mineral chemistry, lithophile element bulk chemistry and Sm-Nd isotopic systematics suggest that ureilites were highly fractionated igneous rock of either magmatic cumulates or partial melt residues accounting for the basalt-depleted remains that form the ureilite meteorites from a differentiated

achondrite parent body (Weisberg et al., 2006). However, the O-isotopic compositions do not follow a mass-dependent fractionation trend which is characteristic of planetary differentiation, due to ureilites plotting along the CCAM (this line suggests a possible relationship to the CV chondrites) (Weisberg et al., 2006). The high carbon content and similar oxygen isotope ratios or ureilites and carbonaceous chondrites such as Cos and CVs, as well as their high Zn and refractory siderophile elements abundances, have hinted at a relationship between ureilites and carbonaceous chondrites (Dodd, 1981). The heterogeneous O-isotope ratios combined with these characteristics are unlikely to have survived extensive geological processes of the parent body, such as carbon which contains planetary-type noble gases and metals that have a high abundance of trace siderophile elements suggesting that ureilites could represent the mantle of a partially differentiated parent body (Downes et al, 2008; Goodrich, 1992; Nestola et al., 2020). The heterogeneity of oxygen isotope ratios in the ureilites has also been proposed to reflect the number of parent bodies that the ureilites originated from. As if the ureilites are homogenised during differentiation heterogeneity could be explained by multiple parent bodies that accreted similar materials and formed via similar processes that were common in this region of the early Solar System (Downes et al., 2008). Modern theories of the UPB indicate there is only a single UPB based on the olivine populations of both polymict and unbrecciated ureilites showing similar Mg#, the similarity is unlikely to occur if unbrecciated ureilites were derived from a range of different parent bodies (Downes et al., 2018).

In either case, ~4.56Ga U-Pb age and recent studies of short-lived chronometers indicate that the parent asteroid of the ureilites differentiated or partially differentiated very early in the history of the Solar System. A total data set for 45 ureilites of all types now averages 0.30 wt% Al which is low in comparison to the chondritic parent material or in comparison to the average for aubrites (highly reduced achondrite meteorite). The consistently low Al contents of ureilites have led to the suggestion that the basaltic component of the parent asteroid was efficiently lost by a process of explosive volcanism (Warren et al., 2006).

The minerals within ureilites exhibit evidence of shock deformation including silicate darkening undulose extinction and irregular fractures. Silicate darkening is caused by the dispersion within silicate grains of 10-5000 μm long curvilinear trails composed of 0.2-4 μm blebs of metallic Fe-Ni and accessory sulphide. Both olivine and pigeonite grains in ureilites contain such trails. Most ureilite olivine grains exhibit undulose extinction and possess

irregular fractures. These shock microstructures are constant with shock stage 2 and indicate a peak shock pressure of <4-5 Gpa (Rubin, 2006; Stöffler et al., 2018).

The thermal shock histories of the ureilites are also divided into four periods. The first is referred to as formation when ureilites formed via melting of chondritic material; the second is the initial shock stage caused by impact events that resulted in silicate darkening, undulose to mosaic extinction in olivine and diamond formation; the third is post-shock annealing; and the final stage is thermal shock referred to as post-annealing shock where some ureilites were shocked again to form a polymict breccia (Rubin, 2006).

Carbon abundances are notably high in ureilites, ranging up to 8.5 wt% with the carbon occurring principally as graphite. It is this distinctive high abundance of carbon that separates ureilites from other achondrite meteorites due to the presence of graphite and diamond between silicate grains (Nestola et al., 2020; Nabiei et al., 2018). The carbon-rich matrix phases in ureilites have a variety of forms (Berkely et al., 1980). The carbon is typically graphite and is proposed to be a late-stage addition and linked to the presence of reduction rims in silicate minerals and core-rim disequilibrium potentially caused by oxidisation/reduction reactions involving C-CO-CO_2 system or methane (Day et al., 2017). The carbon infiltration likely occurred after the initial melt depletion either from C-rich fluids or impact event/disruption (Day et al., 2017). Nova 001 and other ureilites contain euhedral graphite laths up to 0.3x1 mm in size some with pyramidal terminations, and interstitial to coarse mafic silicate grains. Although the euhedral graphite grains could be a primary magmatic phase this seems unlikely in a large magma body because of the low density of graphite (2.23 gcm^{-3}) relative to that of ultramafic liquids (>2.85 gcm^{-3}). This would result in graphite flotation unless crystallisation was rapid such as has been inferred for impact melted enstatite (chondrites) or strong convection currents kept the magma well mixed (Goodrich, 1992; Berkley et al., 1980). In addition, the silicates exhibit disequilibrium textures with the graphite as the olivine grains have rims which have been reduced, becoming Mg-rich and hosting blebs of Fe metal (Rubin, 2006).

The ureilites also contain carbon in the form of diamonds. There is substantial debate surrounding the origin of these diamonds. There are three main models for the origin of diamonds: 1. High static pressure in the mantle of a large parent body, 2. Shock pressure, and 3. Chemical vapour deposition (Nabiei et al., 2018; Tomkins et al., 2022). Evidence for high static pressure origin comes from the coarse size of some diamond inclusions within

the meteorite which suggests that they formed through deep mantle processes (Nabiei et al., 2018). Work completed on the Almahata Sitta ureilite known to contain large diamonds along with the inclusion of chromite and Fe-S-P phases suggests that the diamonds could only form at static pressures higher than 20 GPa (Nestola et al., 2020). Another study completed supported that the diamonds formed through shock pressures after data collected from the micro-diamonds of three different ureilite samples showed evidence for formation through a shock event characterised by peak pressure as low as 15 GPa based on the shock level recorded by silicates alongside the Fe-S-P phases associated with the diamonds requiring high static pressure to form (Nestola et al., 2020). While noble gas content led to suggestions that the diamonds formed through chemical vapour deposition in the solar nebula before later addition into the UPB (Tomkins et al., 2022). If diamonds formed by high static pressure ureilite meteorites would provide evidence that other Mercury-Mars-size bodies did once exist in the Solar System. However, other diamonds show signs of plastic deformation as high density of dislocations, stacking faults and a number of {111} deformed twins with grain boundary of the graphite forming parallel to the {111} planes of the diamonds, this has been interpreted to be consistent with shock metamorphism and therefore may have formed during the parent body break up and destruction (Nabiei et al., 2018).

This research focuses on the Nova 001, Reid 016 and Haverö ureilite meteorites.

1.5.1.1 Nova 001

Nova 001 was found in 1991 as one stone of 349g with uncertainty surrounding the discovery location of this meteorite (Wlotzka, 1993). This meteorite was observed to show very little shock (S3) (based on Stöffler et al., 2018 classification) for a ureilite meteorite. Nova 001 is comprised of anhedral equant grains of olivine that comprise 50-70% of the rock. The olivine grains have rims which have been reduced to hold blebs of Fe metal. Other minerals within Nova 001 include pyroxene with small amounts of euhedral graphite, troilite, Ni-Fe metal and diamond (Treiman and Berkley, 1994). No preferred orientation of the silicate grains has been described for Nova 001. The shock features include polygonisation of graphite, possible diamonds, undulatory extinction and fracturing of silicates (Treiman and Berkley, 1994).

Graphite crystals within this meteorite have been observed in the silicate mineral grains which are equant and euhedral, the graphite also has a radiating clasts texture and groups of parallel plates embedded in olivine, this feature is not seen in any other ureilite (Treiman and Berkley, 1994). The presence of graphite crystals in the silicate minerals suggests igneous origin and that a large proportion of silicate magma was present locally while the samples were crystallised in situ (Treiman and Berkley, 1994). The radiating and euhedral texture of the graphite has been explained by a carbon-rich fluid phase where graphite formed before or contemporaneously with the silicate melt. This fluid melt phase will have allowed the graphite crystals to be surrounded by solid silicates (Treiman and Berkley, 1994). Nova 001 has also been significantly weathered in the terrestrial environment with hydrous Fe oxide stains and masses observed along grain boundaries and cracks throughout the silicate grains. And the exterior contains many sand grains (Treiman and Berkley, 1994).

1.5.1.2 Haverö

The Haverö meteorite fell on the 2nd August 1971 and was discovered on the island of Haverö in Finland. The Haverö sample has a brecciated texture along with elongated cavities which are stretched in one direction, the cavities are sometimes infilled with kamacite veinlets, as well as being enriched with carbon in the form of diamond-graphite (up to 0.9 mm) inclusions. Haverö is a recrystallised silicate rock, (Neuvonen et al., 1972; Vdoykin, 1976).

The olivine grains within the Haverö meteorite range in size from 20 to 100 µm. While most olivine grains are equant some are elongated in one direction. The olivine has a reaction rim that is more Mg-rich and contains Fe metal grains while the core is more Fe-rich. The olivine grains show similar crystallographic orientation under the optical microscope (Wlotzka, 1972).

Pyroxene is in higher abundance than other ureilites with the pyroxene appearing as large crystals of clinopyroxene with polysynthetic narrow twinning (Wlotzka, 1972; Nuevoene et al., 1972).

Black veins are observed within the Haverö meteorite, with X-ray diffraction patterns showing lines of graphite, diamond and kamacite (Wlotzka, 1972). Within Haverö, many small grains of low-Ni kamacite were observed, but no taenite. Where metals within Haverö

are found there is a relationship between the metal and black vein in terms of size and distribution of the metal content seen throughout the sample. (Wlotzka, 1972).

1.5.1.3 Reid 016

Australia II is the unofficial name for Reid 016 a 110 g sample found in 1995 in Western Australia, which is a ureilite polymictic breccia (Grossman, 1998). There is a lack of literature which discusses the mineralogy and texture in a specific context to this meteorite, with literature surrounding Reid 016 discussing ureilites as a whole only.

1.5.2 Aubrite Meteorite

The Aubrite meteorite group is the second group studied as part of this research. The Aubrites formed under different conditions to that of other meteorite groups studied within this thesis offering a comparison to formation conditions in a different region of the early Solar System.

Aubrites are fragments of the crust and/or mantle of a parent body which was composed of highly reduced material (Weisburg et al., 2006). Aubrites are enstatite pyroxenites ($MgSiO_3$) that consist mostly of Fe-O free enstatite, the low Fe content of the enstatite minerals as well as the presence of up to 1.2% of metallic silicon which can be found dissolved within rare Fe-Ni grains (Wasson, 1985) indicate that the aubrite formed under highly reducing conditions in a separate part of the solar nebula to other chondrites (Keil, 1989; Rollinson, 2009). Based on the reducing mineralogy and geochemistry seen within aubrites including normally lithophile elements (Ti, Cr, Mn, Na) behaving partly as chalcophiles (sulphides) or partly as siderophiles (Si occurring in Fe and Ni) (Keil, 2010). It has been suggested that the aubrite parent body formed within 1 AU of the Sun or as near to the Sun as Mercury where the hydrogen partial pressure was high (Keil, 2010). This highly reduced mineralogy and oxygen isotope ratio of aubrites has led to the suggestion that they have close affinities to the Enstatite chondrites, with the composition essentially identical to that of EH/EL

chondrites, with aubrites also having the highest metallic concentrations similar to those in EL chondrites. Thus, aubrites have also been referred to as enstatite achondrites (Weisberg et al., 2006; Keil, 2010; Wasson, 1985). Based on the trace element analysis it is believed that aubrites and EH/EL chondrites are linked possibly coming from the same parent body with the aubrites forming by deep igneous processes inside the mantle above the metal core and below the postulated unmelted enstatite chondrite crust (Keil, 2010).

The aubrite parent body is likely to have formed by partial melting with the removal of the melt allowing for continued melting to very high temperatures and crystallising. (Weisberg et al., 2006). Having undergone extensive melting and efficient magmatic differentiation to separate most of the metal from silicates. All aubrites are breccias with the expectation to this being the Shallowater meteorite (Gaffey and Kelley, 2004; Weisberg et al., 2006). It is thought that some aubrites did not form directly from enstatite high (EH) or enstatite low (EL) chondrites on their parent bodies but most likely formed from an enstatite chondrite-like material that was derived from a highly reduced ultramafic and Mg-rich source (Keil, 2010).

Research into aubrite meteorites has been largely focussed on their potential link to enstatite-like materials. Aubrites have been proposed to have originated from the E-type asteroid 44 Nysa based-on similarities between aubrites and 44 Nysa albedo and reflectance spectra that is flat to slightly reddish (Gaffey and Kelley, 2004). Aubrite meteorites likely represent a reduced endmember for differentiated planetesimals (Keil, 2010).

Oxygen isotope data from pyroxenes for aubrite meteorites are compositionally identical to differentiated rocks of the Moon and upper mantle of the Earth with values that are ±0.2% for both $^{18}O/^{16}O$ and $^{17}O/^{16}O$. This suggests that all three planetary bodies derived their oxygen from the same common source and formed from the same reservoir of material in the early Solar System (Mayeda and Clayton, 1980).

The average Si isotope ratio for aubrites is lighter than the non-metallic phases in EH and EL chondrites. This lighter isotopic composition could be a result of the differentiation processes of the aubrite parent body which segregated some Si into Fe metal during the core formation thus driving the composition of the silicate phase towards the heavier isotopic compositions, due to the siderophile nature of heavier Si-isotopes would be drawn to the core compared to that of the lighter isotopes, which would have migrated towards the Earth's

crust (Savage and Moynier, 2013). This differentiation driven isotope fractionation can be produced by partial melting and fractional crystallisation of E-chondrite like material. From this, basaltic material containing plagioclase and enstatite should exist. With regard to the Si content of the aubrites, the kamacite (iron-nickel alloy found within meteorites) Si content is much lower than the EH and EL chondrites this, therefore, indicates a possible partial or total rehomogenisation of Si on the aubrite parent body occurred and isotopically light Si present in the kamacite prior to differentiation has entered the non-magnetic phases thereby driving the non-metallic and non-magnetic phases to lighter composition (Savage and Moynier, 2013). The second hypothesis for the Si isotopes is that magmatic differentiation has affected the Si composition of the aubrites, if formed by partial melting and fractional crystallisation of EC-like material, Si composition of the aubrites has most likely been affected by post accretionary differentiation related processes (Savage and Moynier, 2013). Other results have suggested that aubrites are not from the same parent body as EH/EL chondrites, because most aubrites are breccias or regolith impact breccias containing solar wind-implanted noble gases (Keil, 1989; Keil,2010).

Overall, the aubrite chemistry shown in the petrology, geochemical studies, cosmic ray exposure ages and extinct radionuclide systematics suggests formation as a result of partial or total melting and fractional crystallisation of material similar to that of the E-chondrite parent body with the EH and EL. The reducing mineralogy of all three groups suggests that they formed in close proximity in the solar nebula, and closer to the sun than both ordinary chondrites (OC) and carbonaceous chondrites (CC) chondrites at around 1AU (Savage and Moynier, 2013).

1.5.2.1 Cumberland Falls

The Cumberland Falls meteorite fell on the 9th April 1919 and is classed as an aubrite polymictic breccia (Binns, 1969; Lipschutz et al., 1988). Some notable features of the Cumberland Falls meteorite include the presence of dark chondritic clasts in a white cataclastic matrix of enstatite pyroxene (magnesium end member of pyroxene silicate mineral) (Binns, 1969; Lipschutz et al., 1988). Otherwise, the Cumberland Falls meteorite comprises enstatite pyroxene with small quantities of metal, metallic sulphide and graphite (Merrill, 1920; Rubin, 2010).

The oxygen isotopes of the chondritic fragments (Δ^{17}O% of 0.93%) are inconsistent with a genetic relationship to the enstatite meteorite clan (Δ^{17} O% of EH chondrites 0.010 and EL chondrites 0.014), enstatite meteorites are a group of meteorites rich in the enstatite mineral (Verkouteren and Lipschutz, 1983; Keil, 2010; Newton et al., 2000). Overall, there have been few studies which have taken place looking at the chondritic material within the Cumberland Falls meteorite and classifying the material contained within this aubrite.

All chondritic clasts in the Cumberland Falls appear to be related, inferring that the chondritic clasts are all remanets of the same projectile that impacted the Cumberland Falls region of the aubrite parent asteroid. In the first systematic study of the Cumberland Falls chondritic clasts the mineralogy and petrology indicated that it is a member of a unique primitive chondrite suite 'The Forsterite chondrite group' that condensed from the solar nebula over a board redox range where the redox state is between that of enstatite and ordinary chondrite, with the parent body having impacted an aubrite meteorite parent object causing chondritic material to be severely shocked and rapidly cooled, before incorporation into the aubrite host (Lipschutz et al., 1988). However, subsequent studies presented evidence that the chondritic clasts are ordinary chondrites based on textural similarities, LL chondrite-like bulk chemical composition, presence of barred olivine chondrules and O-isotope data that is in the OC range rather than the inclusions being of enstatite chondrite or carbonaceous chondrite origin (Rubin, 2010), or a new chondrite group.

The Cumberland Falls meteorite also contains clasts of impact melt breccias presumably shocked and melted upon accretion to the Cumberland Falls host, with the chondritic clasts being all that remains of the same projectile that affected the Cumberland Falls region of the parent aubrite asteroid (Rubin, 2010). Hand specimen descriptions of this meteorite note the presence of slickensides while optical microscopy investigations report crushed and optically distorted pyroxenes suggesting that the sample has also undergone metamorphism potentially as part of a fault on the aubrite parent body (Merrill, 1920).

1.5.3 Miller Range Ungrouped Meteorite

The final meteorite group studied within this thesis is an anomalous achondrite which has an affiliation with ureilites, offering a comparison between two similar meteorite groups. There are six similar meteorites which were all found in Miller Range (MIL) mountains that are presently classified as ungrouped achondrites possibly related to brachinites (primitive ultra-mafic olivine-rich achondrite group) these meteorites are MIL 090340, MIL 090356, MIL 090206, MIL 090895, MIL 090963 and MIL 090405. The oxygen isotopic compositions of brachinites and brachinite-like achondrites are noted to be similar to those of HED meteorites (Goodrich et al., 2017). Ungrouped achondrite meteorites are given this classification when they do not fit into any of the current classified achondrites groups.

1.5.3.1 MIL 090356

The classification of the MIL090356 meteorite has been in some debate over the years. MIL 090356 was discovered in 2009 ANSMET field season and was originally classed as a ureilite, due to the olivine grains having carbon-rich rims contain metal and the composition of the cores of olivine and pyroxene grains. However subsequent work reported olivine composition of Fo_{70-73}, which is more ferroan than olivine in known ureilites, leading to the reclassification to an ungrouped achondrite (Singerling et al., 2013; Goodrich et al., 2017; Meteoritical Bulletin, 2012).

It is now however believed that, while remaining an ungrouped achondrite the MIL 090356 is more closely related to the brachinites, another form of an achondrite meteorite. Brachinites are an ultramafic dunitic or wehrlitic unbrecciated and unshocked rock with SiO_2 (~36-39 wt%) and Al_2O_3(~0.2-2.5 wt%) while having high in MgO (~27-30 wt%) and FeO (~26-37 wt%) consisting mostly of olivine; the minerals tend to be homogeneous and textures are medium to coarse grained, with olivine-olivine grain boundaries commonly forming triple junctions. (Keil, 2013).

This link between brachinites and MIL 090356 is made based on the petrology, including the presence of grain boundary symplectites which are ubiquitous throughout the brachinites and are also found within MIL 090356 (Singerling et al., 2013). The symplectities within the MIL 090356 are mostly likely formed from a non-equal mixture of orthopyroxene and

troilite along olivine grain boundaries, with the reaction responsible for the symplectic intergrowth being a sulfurization reaction which occurred post-crystallisation from an infiltrating S-rich gas (Singerling et al., 2013).

1.6 Aims and Objectives

The aim of this research is to measure the petrology and microstructures within the ureilite, a related anomalous achondrite and aubrite achondrite meteorite groups using various SEM techniques such EDS, EBSD and EPMA to gain a better understanding and interpret processes which occurred across their parent asteroid. The expected outcome of the ureilites and aubrites analysis will show two distinct geological histories due to the parent bodies forming in separate parts of the solar nebula while the anomalous achondrite is expected to show some similarities to the ureilites as it shares many petrographic similarities but also contain some deviation which should be detected.

The overall outcomes this study aims to achieve is to further understand the microstructures and petrology of the samples. By interpreting these textures this thesis will add to the current understanding of the early planetary processes within the Solar System and evidence possible similarities between meteorite groups within similar regions of the solar nebula, as well as highlighting the differences that exist. The purpose of this research is to provide a deeper understanding into the processes that occurred in different regions of the early Solar System and links between the meteorite groups.

2. Methodology

2.1 Sample Selection and Preparation

The samples that have been studied are ureilites: Reid 016, Haverö, Nova 001; aubrite: Cumberland Falls and an anomalous achondrite: MIL 090356. These samples were chosen for this study as they span a range of petrologies and characteristics within achondrite meteorites. This sample suite allows for comparison between each group. Each of the samples are polished thick sections, placed on block face pin mounts while being prepared in line with the sample preparation guidelines at the Smithsonian Institute. Each of the samples were further polished at the University of Glasgow for scanning electron microscopy (SEM) imaging, and EBSD mapping.

The method of polishing used was to first smooth the surface of the sample using a 1 micrometre (μm) grade of colloidal aluminium suspended in glycol for five minutes followed by 0.3 μm colloidal aluminium suspended in glycol for another five minutes. The samples are then placed on a vibromet polisher with 100 nm colloidal silica suspended in a sodium hydroxide solution to chemically abrade the sample surface to remove the mechanical damage layer producing the high-quality surface required for EBSD. The samples were then coated in 10 nm of carbon for EDS. The carbon coat was then removed, through polishing and replaced with a 7 nm thick layer of carbon for EBSD. Carbon was used to conduct the charge of the electron beam away from the sample surface to produce a clear image.

The samples were analysed using SEM imaging, quantitative EDS, as well as EDS and EBSD mapping using a Carl Zeiss Sigma Variable Pressure Field Emission Gun Analytical Scanning Electron Microscope at the Imaging Spectroscopy and Analysis Centre (ISAAC) at the University of Glasgow (Fig.2). The samples were also analysed using Electron Probe Microanalysis (EMPA) using the JEOL-JXA 8530F EPMA at the Smithsonian Institute.

Figure 2: The Carl Zeiss Sigma Variable Pressure Analytical Scanning Electron Microscope housed in the Imaging Spectroscopy and Analysis Centre (ISAAC) at the University of Glasgow.

2.2 Scanning Electron Microscopy

An SEM is designed primarily for imaging, using a focused high energy electron beam to generate a variety of signals at the surface of solid specimens (Reed, 2005; Swapp, 2017). The signals collected from the interaction between the electrons and the sample reveal information on the texture, chemical composition, crystal structure and orientation making it an effective way of studying solid samples (Swapp, 2017). Electrons in the SEM are held in a negative potential, typically at 10-30 keV with the use of an emitter most commonly a tungsten filament about 0.1 mm in diameter. Electrons are accelerated towards the sample through the electron gun and lens (column) the purpose of the electron gun is to accelerate the electrons towards the sample, carrying significant amounts of kinetic energy which is dissipated through the sample providing a range of signals to be produced by interactions

when the incident electrons impinge upon the sample (Reed, 2005; Swapp, 2017). In the SEM analysis, chamber air is evacuated to produce a vacuum using a vacuum pump and compressor, a high vacuum of 10^{-6} bar is created, once the vacuum is established the electron beam is brought into focus on the sample surface to allow for a clear image to be created for analysis.

The atom density changes at the specimen surface abruptly due to the very high density of the solid relative to the vacuum. Where the electron beam interacts with the atoms in the specimen's surface through a variety of physical processes is referred to as a scattering event. When accelerated primary electrons enter a solid, they scatter both elastically (by electrostatic interaction with atomic nuclei) and inelastically (by interaction with the atoms electrons in its electron shells). These interactions produce secondary electrons (SE), backscattered electrons (BSE) and characteristic X-rays (Goldstein, 2003; Swapp, 2017; Egerton, 2005) (Fig.3). The characteristic X-rays can be used to identify and quantify the elements present within the interaction volume (Goldstein, 2003).

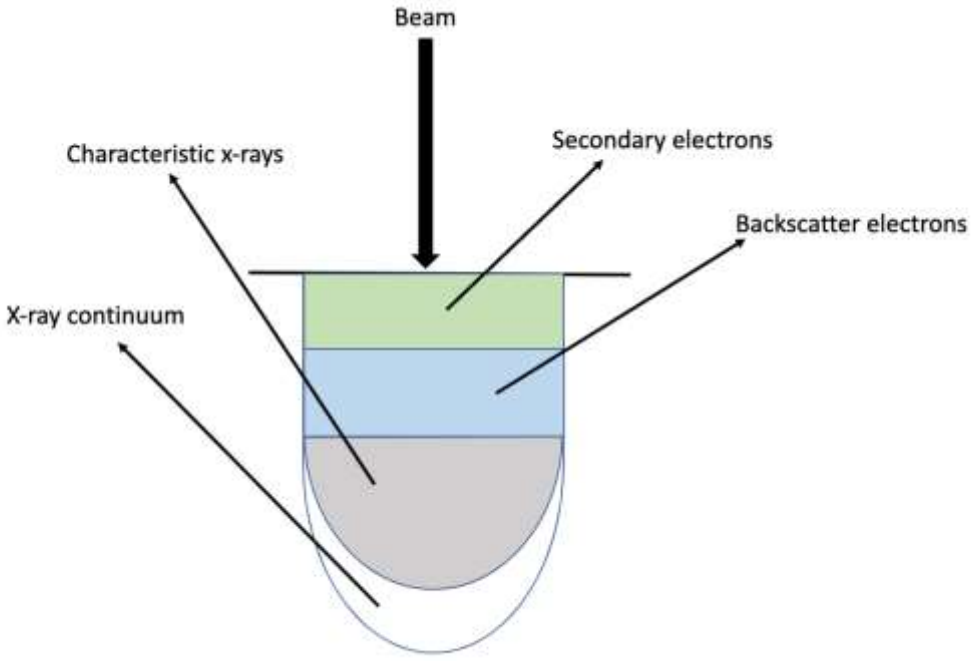

Figure 3: Range of signals that can be produced by the interaction of the electron beam with the sample. Secondary electrons can also be produced from backscatter electrons as well as the incident beam. Adapted from (Zhou et al., 2006)

2.3 Aztec Data Analysis

For this project, the AztecFlex software package from Oxford Instruments was used for the data analysis. Specifically, AztecCrystal 2.1 was used for the EBSD analysis while AztecOne 5.1 was used in the analysis of the SEM and EDS data.

The measuring tool within AztecOne was used to obtain data on the fracture widths within the ureilites and anomalous achondrite. RGB false colour images were also created within AztecOne to highlight the distribution of magnesium, carbon, and iron to better show the petrology of each sample. The difference between the carbon found within the sample and the resin used to coat the samples was identified by the texture of the carbon present (Fig.4).

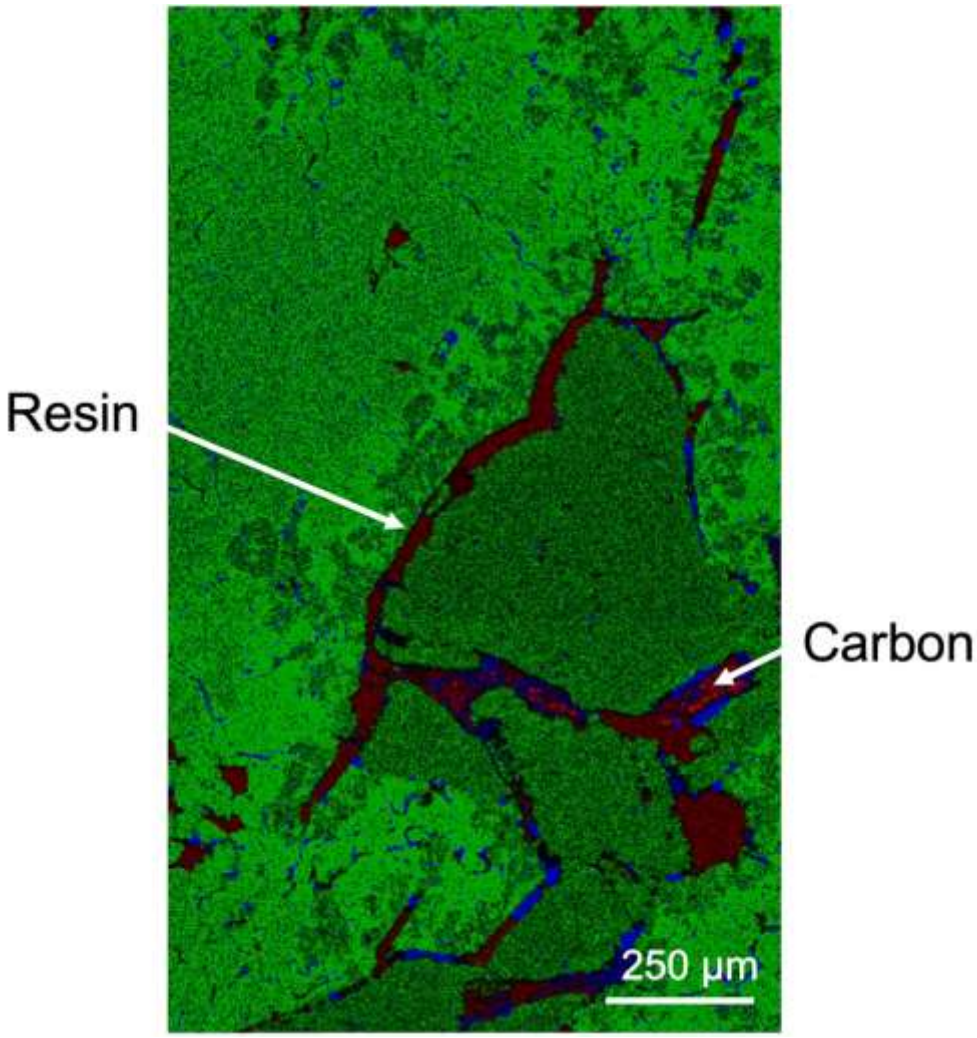

Figure 4: False coloured EDS layer montaged image map (Red: Carbon, Green: Magnesium, Blue: Iron) demonstrating the comparison between the types of carbon found within the meteorite samples of this thesis. Shows carbon as an element within the sample, demonstrating an uneven texture and the resin which appears within the sample with a lack of texture and smooth appearance due to the polishing and preparation of the sample.

2.4 SEM Imaging

In petrology, SEM imaging is a non-destructive technique (Reed, 2005). An SEM's primary design is for imaging, these images are produced by a beam of electrons which is rastered across the surface of the sample. These electrons interact with the sample producing a variety of signals that can be collected by bespoke detectors to provide specific information about the sample (Reed, 2005). SEM can produce BSE images of polished sections which show differences in mean atomic number density. The signal is produced by elastic scattering from the deflection of the incident electron with the atomic nuclei or outer shell electron of similar energy, the incident electrons that are inelastic scattered at an angle of 90º or more are referred to as backscatter electron (BSE) (Zhou et al., 2006; Reed, 2005). These images are very useful both in sedimentary and igneous petrology to show the specimen composition, topography, mass thickness and crystallography (Goldstein et al., 2018).

2.5 EDS Imaging

EDS X-rays are produced when the electrons within the electron beam are slowed down when they reach the solid sample. This interaction between the bombarding electrons and the outer shell electrons of atomic nuclei excites the outer shell electrons which when they return to a ground state emit an X-ray photon with a specific energy. These photons are emitted with sharply defined energies that are specific to each atom/element species (Fig.5) (Reed, 2005; Goldstein, 2003). The X-rays are then collected by an EDS detector where the energy spectra are identified. The number of X-rays collected is related to the relative abundance of each element in the sample.

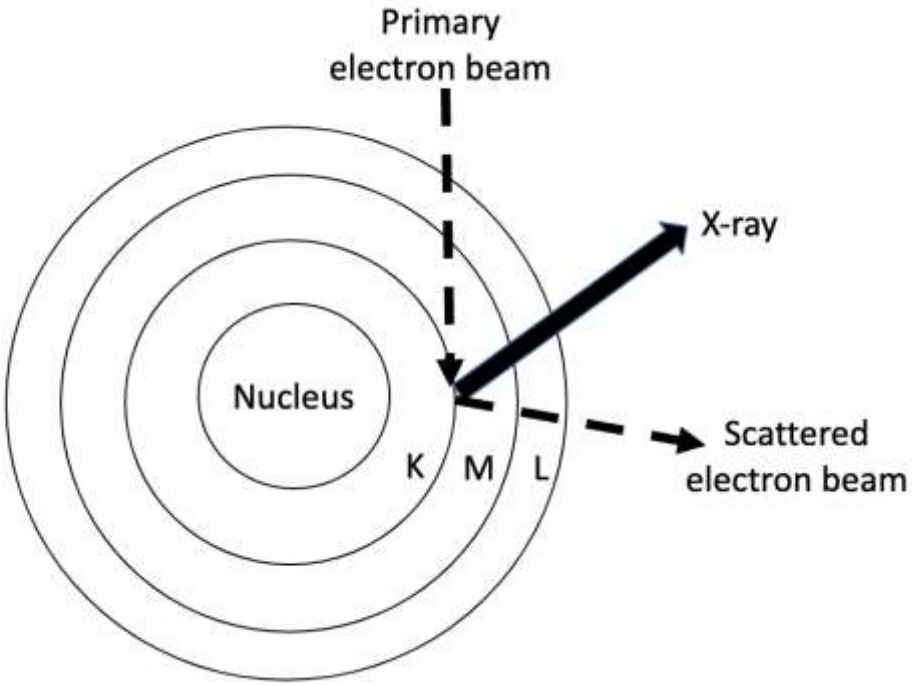

Figure 5: Simplified atom model showing the K-L electron orbitals. When the primary electron beam interacts with the electrons the outer shell electrons are excited to a higher energy state when they ground themselves, they release a characteristic X-ray.

EDS data was collected using the Zeiss Sigma Variable pressure field emission gun SEM at the University of Glasgow. EDS data were collected at a working distance of 8.5 mm with an accelerating voltage of 20 kV, an aperture size of 60 µm and a beam current of 1.3 nA. The electron beam was fired at the sample surface at an angle of 0° allowing for the collection of an undistorted image. EDS data were collected using an Oxford Instruments 80-mm^2 X-Max silicon drift detector energy-dispersive spectrometer. EDS data were processed using the Aztec Flex software from Oxford Instruments, within Aztec, false colour EDS maps were generated with the use of the colour bar to assign the following: red: carbon, green: magnesium and blue: iron forming the false colour images used throughout this thesis.

For the bulk composition of the minerals present within each of the samples, an average was taken using a 100 by 100 grid overlayed on each of the samples with each point being assigned a mineral to provide an overall average bulk mineral percentage for the major mineralogy of each sample, while the wt % spectrum function of Aztec was used to note the presence of minor elements within each of the samples.

The grain size was also collected for olivine and pyroxene grains for each sample as well as the width of the iron-rich metal veining and carbon regions using the measuring tool available within the EDS setting to measure the long axis for the olivine and pyroxene grains and diameters of the iron-rich veining and carbon regions.

For the quantitative EDS the electron beam was calibrated against copper while the beam energy was measured using a faraday cup, the EDS spectra were standardised to olivine and pyroxene reference materials and calibrated to known abundances of magnesium, iron and silica for the analysis. Quantitative EDS point analyses were collected for the Cumberland Falls samples with data being collected from across each region of the sample and included measurements of the matrix and chondrules present within the chondritic clast.

2.6 EBSD Imaging

Electron backscatter diffraction (EBSD) is another SEM-based characterisation technique. EBSD enables the characterisation of crystalline materials and can be used to extract textural information such as induvial grain orientation, point to point orientation correlations, internal misorientations and phase identification. EBSD is based on the analysis of diffraction patterns. These diffraction patterns are formed by the primary beam interacting with the crystal lattice of a well-polished sample that has been tilted to a high angle typically 70°. The incident electrons only penetrate approximately 20 nm deep into the specimen (Schwarzer et al., 2009) where they are channelled along the crystal lattice planes. When the channelled electrons impinge upon a phosphor screen (used to collect the diffraction patterns (Wallis et al., 2019; Maitland and Sitzman, 2006)) placed a short distance from the tilted sample in the path of the diffracted electrons a Kikuchi band is formed. A set of Kikuchi bands forms a Kikuchi pattern that can be used to identify the crystal structure and orientation of the phase being measured. EBSD maps visualise the distribution of diagnostic X-rays generated by the rastering of the electron beam across the sample and are therefore an excellent way of visualising the distribution and abundance of chemical elements within the sample (Reed, 2005).

EBSD enables systematic measurement of individual crystallographic orientations that can be used to study microstructures, internal textures, point to point orientation correlations, phase identification (Halfpenny, 2010). Pole figures are most commonly used for the texture analysis, for confirming single crystal orientation and for study slip systems. Inverse pole figure orientation maps use basic RGB colour scheme for cubic phases full red, green, blue is assigned to grains <100>, <110>, <111> axes parallel to the projection direction of the inverse pole figure (Halfpenny, 2010; Maitland and Sitzman, 2006). Data for the grain orientation Euler angle convention was used, the Euler angles describe a minimum set of rotations that can bring one orientation into coincidence with another. The grain size analysis uses changes in the crystallography orientation between neighbouring grid points of greater than a pre-defined minimum that is typically 10º (Maitland and Sitzman, 2006).

EBSD data was collected using the Carl Zeiss Sigma Variable Pressure Field Emission Gun Analytical Scanning Electron Microscope at the University of Glasgow facilities with the EBSD detector attached the measurements used for the SEM setup for the data collection was a working distance set to 15-16 mm, accelerating voltage of 20 kV, an aperture size of 100 µm and the beam current set to 8.9 amps, with the plate placed at an angle of 70° for all EBSD maps. EBSD data were collected using an Oxford Instruments NordlysMax^2 EBSD detector. EBSD data were processed using the Aztec Crystal software from Oxford Instruments. EBSD data was cleaned by first using auto clean-up option of the Aztec software with a further clean-up using an iterative five neighbour correction for each sample were processed using the orthorhombic symmetry, an omega angle to 180º. Data were plotted on pole figures as directions rather than planes. Crystal rotation axis diagrams were generated in crystal co-ordinates and set to plot only data with a 2–10-degree misorientation. The grain distribution was presented as Grain Reference Orientation Deviation (GROD) angle and Kernel Average Misorientation (KAM) maps which used a subset that were generated to include each induvial grain within the sample allowing followed by producing a one point per grain subset to be generated to produce a texture analysis that is unbiased by large crystals.

It should be noted that for this thesis EBSD data was collected only for the Reid 016 and MIL 090356 samples, due to the time and resources available within the scope of this project.

2.7 Electron Probe Microanalysis

Electron probe microanalysis (EPMA) is a technique used typically for chemically analysing small areas of solid material, however, can analyse large areas and maps if time allows (Reed, 2005). EPMA makes use of X-ray spectrum emitted by a solid sample (Fig.3) bombarded with a focused beam of electrons to obtain a localised chemical analysis (Potts et al., 1995). Electron probe analysis is a standard technique in mineralogy and petrology due to its capability for rapid non-destructive in situ analysis of a materials chemistry with a simple specimen preparation requirement (Potts et al., 1995).

EPMA data acquired for sample MIL 090356 was completed using a JEOL-JXA 8530F EPMA at the Smithsonian Institute, Washington, USA. EPMA spectra were collected with an accelerating voltage of 15 kV and a beam current of 69 μA. The elements that were measured and quantified using standard reference materials by EPMA were Fe, Ca, Ti, Mn, Ni, Cr, Si, Al, Mg, Na, S, P, K and O (Table 3).

Table 3: Table listing which standards were used for each element during the collection of the EMPA data.

Element	Standard
Fe	Troilite
Ca	Diopside
Ti	Ilmenite
Ni	Nickel
Mn	Manganite
Cr	Chromite
Si	Anorthoclase
Al	Bytownite
Na	Anorthoclase
Mg	Olivine
S	Troilite
P	Fluorapatite
K	Anorthoclase

3. Results

3.1.1 Ureilite

3.1.1.1 Reid 016 Petrology

Reid 016 EDS false colour images (Fig.6a) indicate that the overall area % mineralogy consists mainly of coarse-grained (average grain size: 0.65 mm) olivine (66%) and clinopyroxene (12%) (average grain size: 0.45 mm) with minor amounts of iron metal (17%) and carbon (5%), of all the grain in the sample the overall grain shape is elongated and sub-angular with a maximum and mean orientation spread of and 17.6º and 3.0º. The EDS sum spectrum wt% of Reid 016 yielded a chemical composition of oxygen (38.6%), magnesium (21.6%), iron (17.9%) and silicon (17.9%) with Aztec wt % spectrum excluding the resin showing minor amounts of Cr, Mn, Al, S and Ni.

Reid 016 also shows reduction rims of the olivine grain (Fig.7), which consists of being Mg-poor within the cores and Mg-rich on the edges of the grains themselves, these rims also contain Fe-metal grains. The rims of varying thicknesses across all the grains of the sample from 4 mm to 16 mm.

Another characteristic of the ureilite mineralogy which can be clearly seen studying Reid 016 is the inclusion of carbon likely in the form of graphite and/or micro-diamond (McSween,1987) (Fig.6b) within anhedral regions within the sample as well as iron-rich metal (Fig.6c). The emplacement of iron-rich metal and carbon in the sample appears to infill fractures (Fig.6a) that have formed across the sample, therefore, for the purpose of this thesis these fractures which have been infilled with carbon and/or Fe-rich metal shall be referred to as veining/veins where appropriate for the remainder of the thesis.

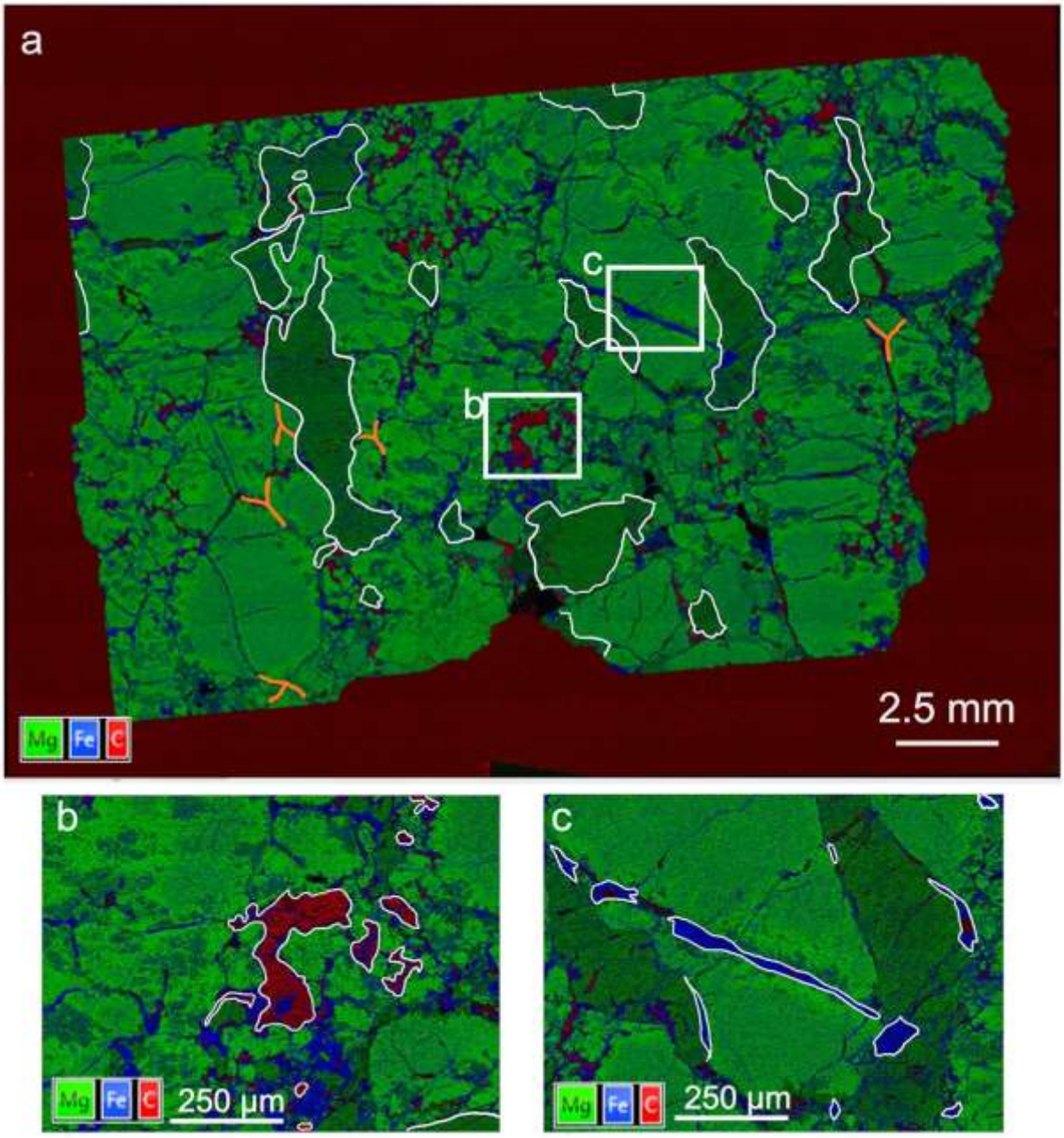

Figure 6: (a) False-coloured EDS layer montaged image map of the bulk composition for Reid 016 (Red: Carbon, Green: Magnesium, Blue: Iron). The white outlined areas represent the pyroxene grains which are of a darker green compared to that of olivine with the white boxes a and b representing the close-up areas of carbon and iron present in the sample the orange showing the 120º triple junctions present. The iron-rich metal appears as veins infilling fractures in the olivine and pyroxene grains, with carbon forming in regions most likely in the form of graphite and/or diamond. (b) False colour EDS image (Red: Carbon; Green: Magnesium; Blue: Iron) of a carbon region (outlined in white) with iron present towards the base of the image within Reid 016. (c) False colour EDS image (Red: Carbon; Green: Magnesium; Blue: Iron) of the iron veining (outlined in white) present in Reid 016. The vein infilling a fracture that formed a boundary of two olivine grains with the iron-rich metal also collecting around the pyroxene grain which surrounds the olivine grains with these grains showing the presentence of reduction rims within the sample.

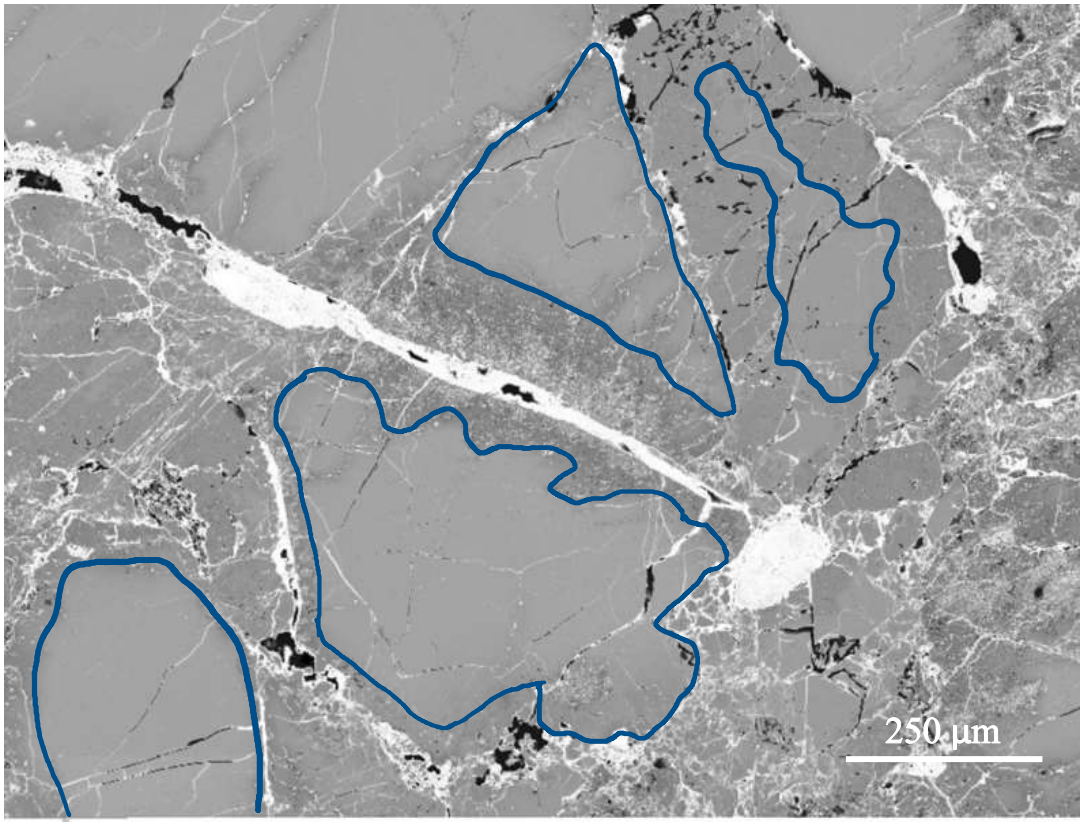

Figure 7:BSE image of the rims observed within the olivine grains of the Reid 016 causing Mg-poor cores (light grey) and Mg-rich rims (dark grey). The blue outlines the edge of the rims within the olivine grains, the white represents the iron-rich metal and the black the carbon.

3.1.1.2 Reid 016 Microstructures

Microstructures observed in the EDS images of Reid 016 are anhedral regions carbon which has an average thickness of 0.068 mm (n=14) while the iron-rich metal veining holds an average thickness of 0.02 mm (n=12), the iron-rich metal veining can be seen infilling fractures that cut between grain boundaries of the olivine and pyroxene as well within the individual grains themselves. BSE image of Reid 016 highlights the interaction of carbon and iron-rich metal with the olivine and pyroxene grains (Fig.8). The olivine grains exhibited 120º triple junction grain boundaries and signs of stage 2 shock with the fracturing of the silicate grains (Fig.6a).

Reid 016 also lacks faults or displacement of the grains in the sample, however, there is a specific preferred orientation along the long axis which can be observed in Figure 6a, while the pole figures of Figure 8 shows a cluster along the <100> axis.

EBSD microstructural analysis of Reid 016 using a grain reference orientation deviation (GROD) angle map (Fig.9a) shows that olivine and pyroxene grains along a central band that cuts across the sample exhibit a high degree of internal deformation of 6-10° whereas the rest of the sample olivine and pyroxene grains exhibit a lower degree of internal deformation of 0-5°. The kernel average misorientation (KAM) map (Fig.9b) shows pixel-pixel misorientations of 0-3°. While the areas with the highest degree of misorientation in KAM maps match the areas of high internal deformation found in the GROD angle map. Comparing olivine to pyroxene reveals that pyroxene grains in Reid 016 exhibit higher internal misorientations than olivine. Where olivine is in contact with a vein, these areas show higher internal misorientation up to 3º relative to the rest of the crystal. The Grain Orientation Spread (GOS) and Mean Orientation Spread (MOS) for the olivine grains in Reid 016 show that GOS is 2.37º and the MOS is 20.29º.

Contoured one-point per grain pole figures for olivine (Fig.10) reveal a point cluster in all three crystallographic axes (<100> <010> <001>) along the major axes being orthogonal to one another. This crystallographic orientation data is consistent with a lineation fabric. Inverse pole figure and Euler maps reveal that most olivine crystals have similar colouration suggesting a moderate to strong crystallographic alignment (Fig.10). Crystal rotation axis diagrams in crystal coordinates show that deformation is accommodated predominantly by a rotation around the <100> plane (Fig.10).

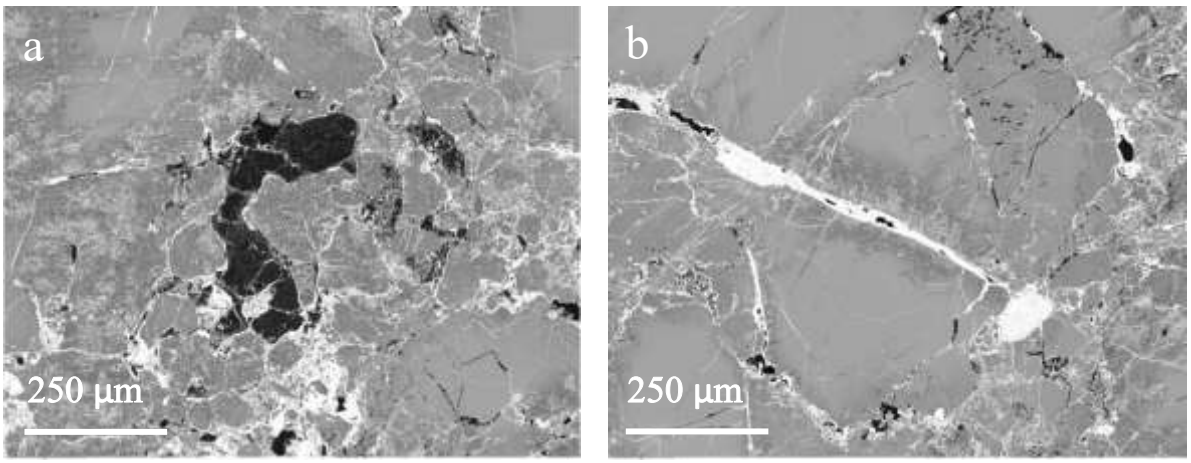

Figure 8: BSE images of a carbon region and iron-rich metal veining within the olivine and pyroxene grains of Reid 016. (a) Demonstrating the carbon (black) rich region located in the centre of the image surrounded by olivine grains with some iron present. (b) Iron-rich metal (white) cutting through the olivine grains in the centre of the image as a vein with smaller veins infilling space between other grains and within grains themselves.

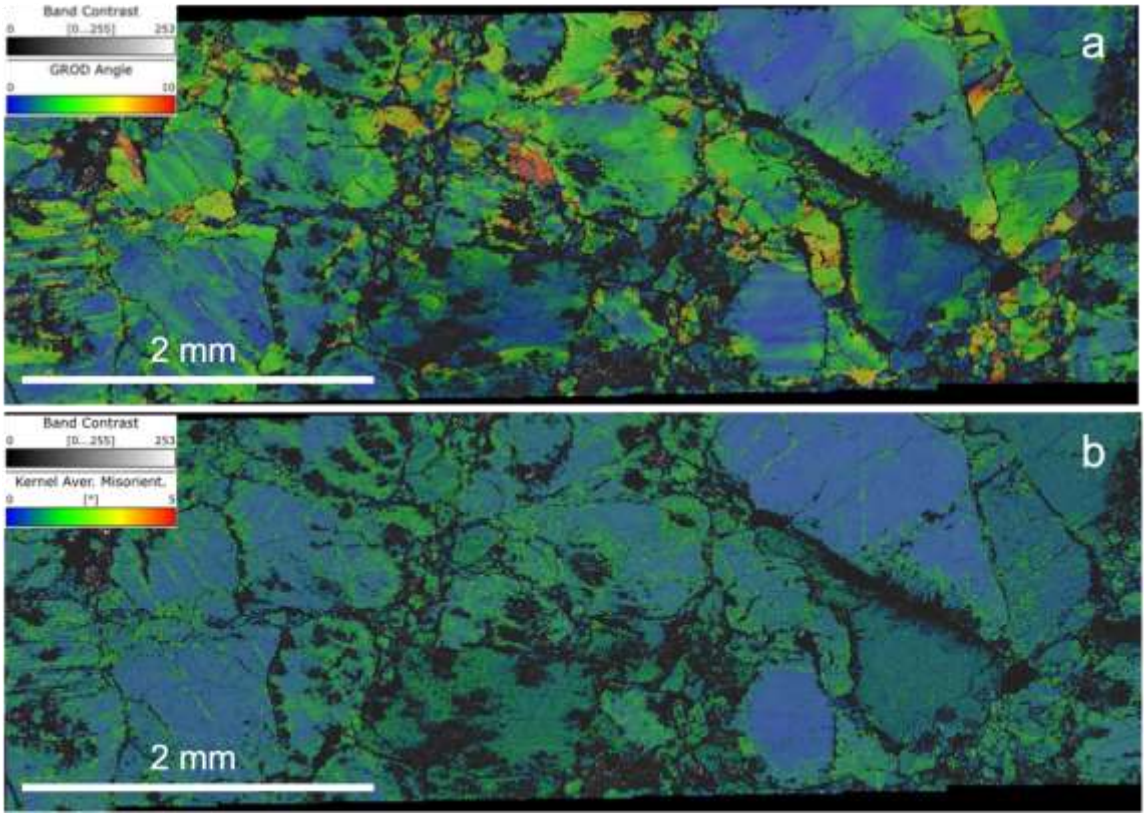

Figure 9: (a) GROD angle map taken from the middle section of the Reid 016 sample with undeformed crystals in blue to those that see an increased internal deformation highlighted through the progression of colours from green to yellow through to red. The maximum amount of internal deformation is located within the smaller grains being highly deformed (red), while the cores of the larger grains (blue) are less deformed. (b) KAM map from the same section of Reid 016, the highest amounts of misorientation is up to 3º with the misorientation appearing across the whole of the sample, with cores of larger grains expressing low amounts of misorientation.

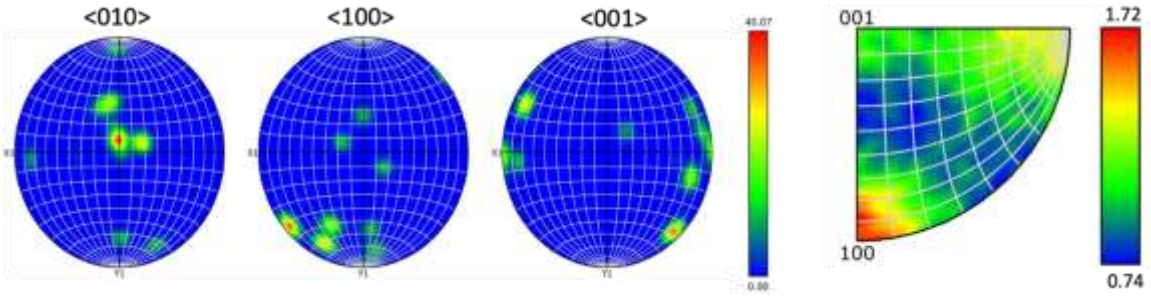

Figure 10: Pole figure diagram (left) for olivine grains plotting one point per grain for a count of 38 crystals across the entire data set for Reid 016. <100> <010> <001> axes all exhibit a point cluster of crystallographic orientation data and the point clusters for each major axis are orthogonal to each other consistent with a lineation of the fabric. The crystal rotation axis diagram (right) shows a strong cluster of rotation around the <100> axis with a moderate cluster around the <010> axis.

3.1.2.1 Nova 001 Petrology

Nova 001 is rich in olivine (56%) (average grain size: 0.60 mm) and pyroxene (24%) (average grain size: 0.5 mm) with lesser amounts of carbon (10%) and iron metal (10%) based on the area % mineralogy of the sample. EDS false colour image of Nova 001 (Fig.11a) shows both the olivine and pyroxene grains are sub-angular. Carbon is present as anhedral regions within the pyroxene grains in some cases within the sample (Fig.11b), the carbon found in Nova 001 is likely to be in the form of graphite/micro-diamond (Nabiei et al., 2018). Meanwhile iron-rich metal is also present in the form of veins that form along grain boundaries, with some veining of the iron-rich metal appearing within the grain (Fig.11c).

The bulk wt % composition determined from an EDS sum spectrum of the whole of Nova 001 sample excluding the resin shows a chemical composition containing oxygen (41.6%), magnesium (20.8%), iron (15.7%) and silicon (19.5%) with minor amounts of Ca, Cr, Mn and S.

BSE maps of Nova 001 reveal that olivine also exhibits reduction rims (Fig.12) the core of the olivine grains is relatively Mg-poor, and the rims are Mg-rich. The reduction rims observed around the olivine grains vary in thickness across the sample, with an average thickness of 0.085 mm (n=12).

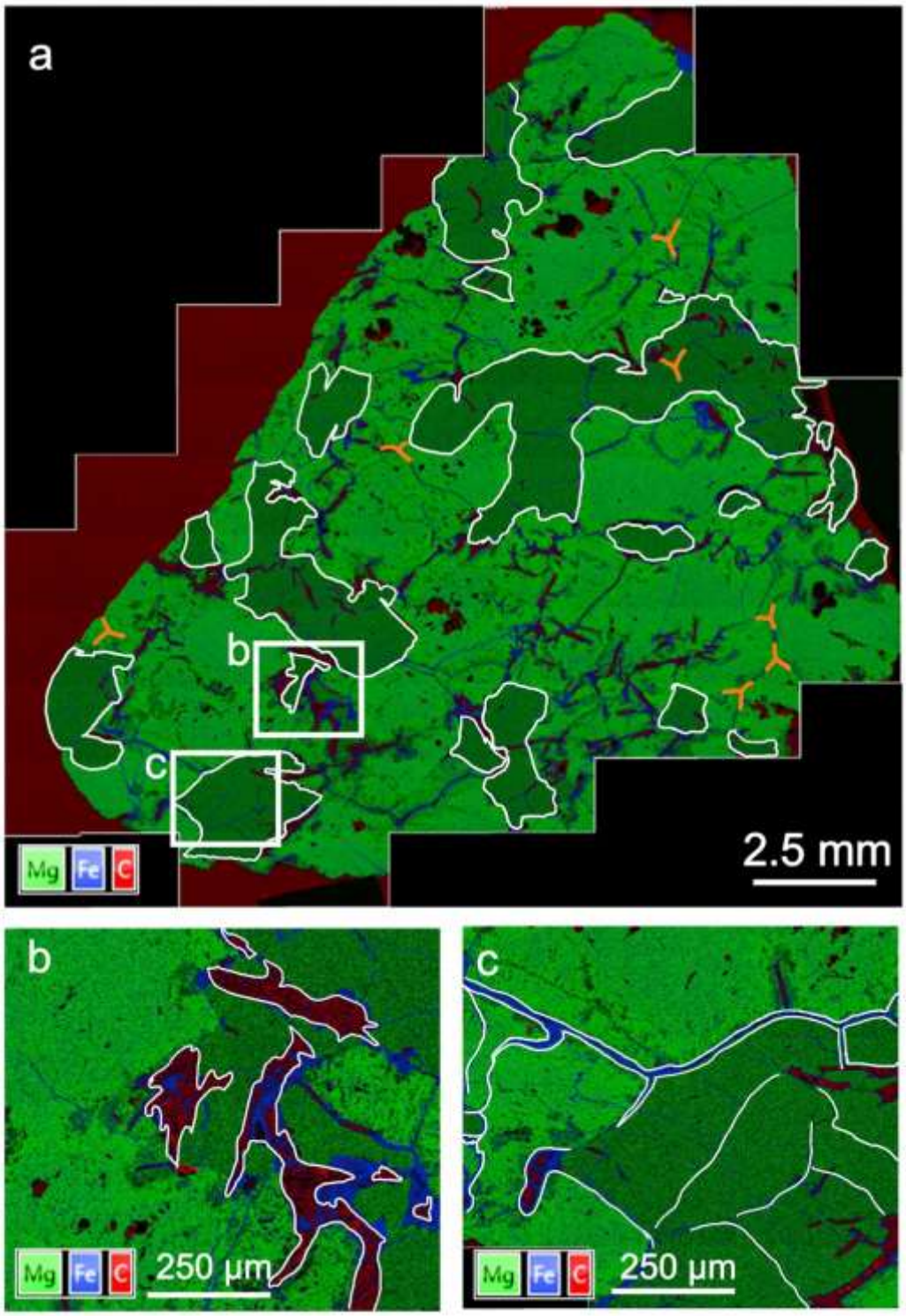

Figure 11: (a) False coloured EDS layer montaged image map of the bulk composition for Nova 001 (Red: Carbon, Green: Magnesium, Blue: Iron). The white outlined areas represent the pyroxene grains which are of a darker green compared to that of olivine with the white boxes a and b representing the close-up areas of carbon and iron present in the sample and the orange showing the 120º triple junctions present. The iron-rich metal appears as veins infilling fractures in both the olivine and pyroxene grains, with carbon present most likely in the form of graphite and/or diamond. (b) False colour EDS image (Red: Carbon; Green: Magnesium; Blue: Iron) of a carbon region (outlined in white) in the centre of the image with iron surrounding the carbon as well as the pyroxene grain, (c) False colour EDS image (Red: Carbon; Green: Magnesium; Blue: Iron) of the iron veining (outlined in white) present in Nova 001. The thicker veining follows the boundary of the olivine-pyroxene grain with thinner veins cutting within the pyroxene grain alongside minor amounts of carbon.

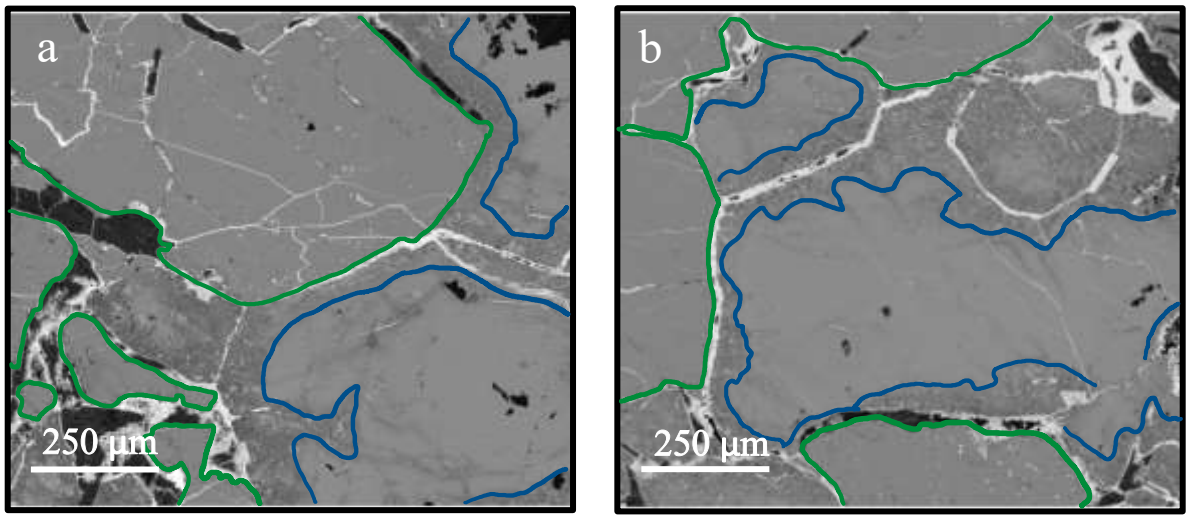

Figure 12: BSE image of the rims observed within the olivine grains of the Nova 001 causing Mg-poor cores (light grey) and Mg-rich rims (dark grey). The green outlines the pyroxene grains with the blue representing the edge of the rims within the olivine grains, the white represents the iron-rich metal and the black the carbon. (a) Shows the rim present in the olivine in the lower right of the image, while the pyroxene grain is seen with the iron-rich metal veining cutting through the grain itself as well as carbon regions present at the grain boundaries. (b) Rims of the olivine grain with iron-rich metal veining separating the grains located in the centre of the image surrounded by pyroxene grains.

3.1.2.2 Nova 001 Microstructures

Within Nova 001 the BSE image shows iron-rich metal throughout the sample in the form of veining (Fig.13b). The veining can be observed cutting through the pyroxene grains with an average thickness of 0.007 mm (n=12), meanwhile, the veining of the olivine can be observed between the boundaries of olivine grains with an average thickness of 0.015 mm (n=12), with finer veining observed cutting through the olivine grains (Fig.13b). The olivine grains, however, do still exhibit 120º triple junction grain boundaries as observed in Figure 11a, while the fracturing of the silicate grains showing evidence of shock stage 2.

The other formation found in Nova 001 of note is the carbon presenting as anhedral regions within the sample (Fig.13a) observed predominately at the boundary between the olivine and pyroxene with the average thickness of these areas being, 0.036 mm (n=12) notably larger than that of the iron-rich metal veining. Based on the literature surrounding ureilites and the Nova 001 sample it can be suggested that the carbon in the sample is graphite and/or micro-diamond (Nabiei et al., 2018).

Nova 001 also shows no indication of specific orientation of the olivine or pyroxene grains in the sample, as well as no signs of faulting or displacement being visible (Fig.11a) within the EDS data collected for this sample.

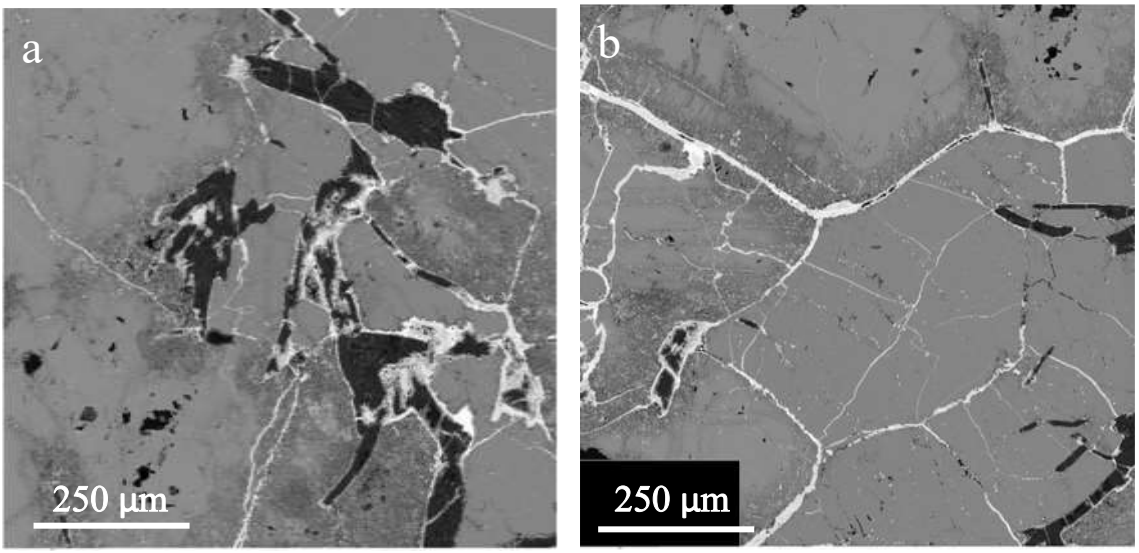

Figure 13: BSE images of the carbon region and iron-rich metal veining that is occurring within the olivine and pyroxene grains of Nova 001. (a) Demonstrating the carbon (black) region located in the centre of the image surrounded by olivine grains, with iron-rich metal interacting with the carbon. (b) Iron-rich metal (white) veining cutting between the boundaries of olivine and pyroxene grains with smaller veins infilling space within the grains themselves.

3.1.3.1 Haverö Petrology

Haverö sample based on the area % mineralogy of the sample is predominantly composed of olivine (80%) (average grain size: 0.73 mm) and pyroxene (6%) (average grain size: 0.5 mm) as well as iron metal (2%) and carbon (12%). The grain shape of both the olivine and pyroxene is sub-angular. The bulk wt % composition determined from an EDS sum spectrum of the whole of the Haverö sample excluding the resin shows a chemical composition containing oxygen (41.8%), magnesium (24.8%), iron (13.7%) and silicon (18.5%) with minor amounts of Ca, Cr and Mn.

Haverö also contains carbon in the form of veining and is likely that this carbon is in the form of graphite/micro-diamond (Fig.14c) (Nabiei et al., 2018). The iron-rich metal occurs as blebs along the olivine-olivine grain boundaries (Fig.14a) and within the grains

themselves compared to the veins observed in other ureilite samples in this thesis, with the addition of reduction rims (Fig.15) observed in the olivine grains, the average thickness of these rims within Haverö is 0.116 mm (n=12).

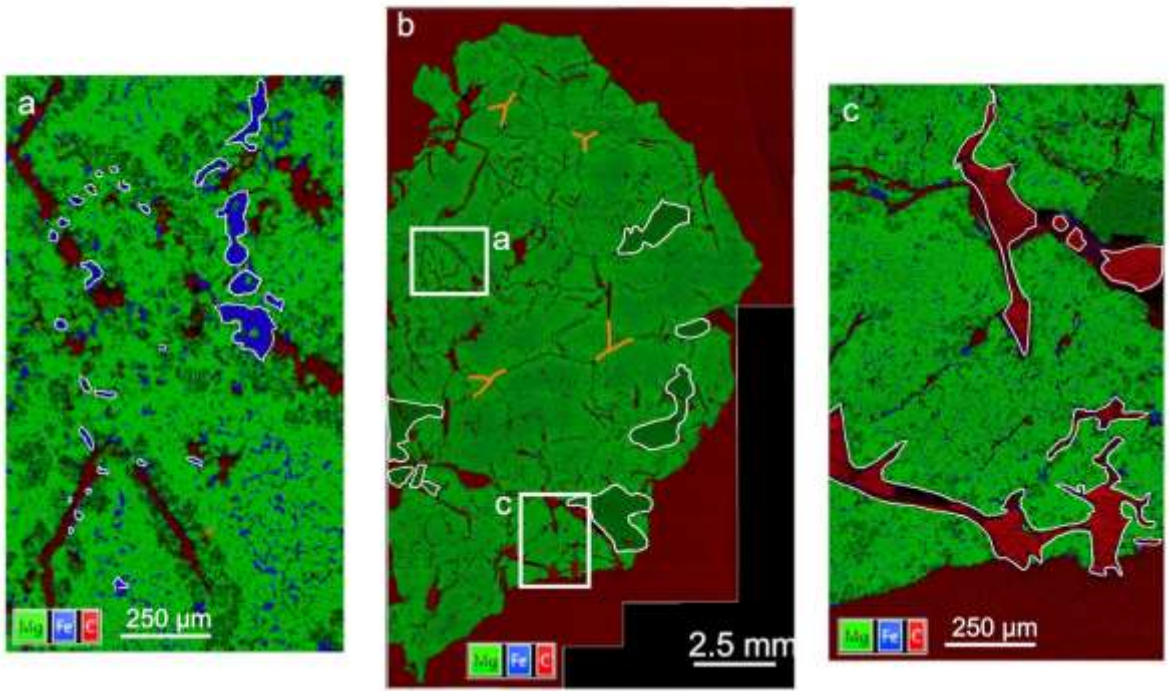

Figure 14: (a) False colour EDS layered montaged image (Red: Carbon; Green: Magnesium; Blue: Iron) of carbon (outlined in white) as veins across the sample between the olivine grains. (b) False coloured EDS layer montaged image map of the bulk composition for Haverö (Red: Carbon, Green: Magnesium, Blue: Iron). The white outlined areas represent the pyroxene grains which are of a darker green compared to that of olivine with the white boxes a and b representing the close-up areas of carbon and iron present in the sample the orange showing the 120º triple junctions present. The iron-rich metal appears as blebs, with carbon-forming veins present most likely in the form of graphite and/or diamond. (c) False colour EDS layer montage image (Red: Carbon; Green: Magnesium; Blue: Iron) of the iron-rich metal (outlined in white) present appearing as small blebs within the olivine grains.

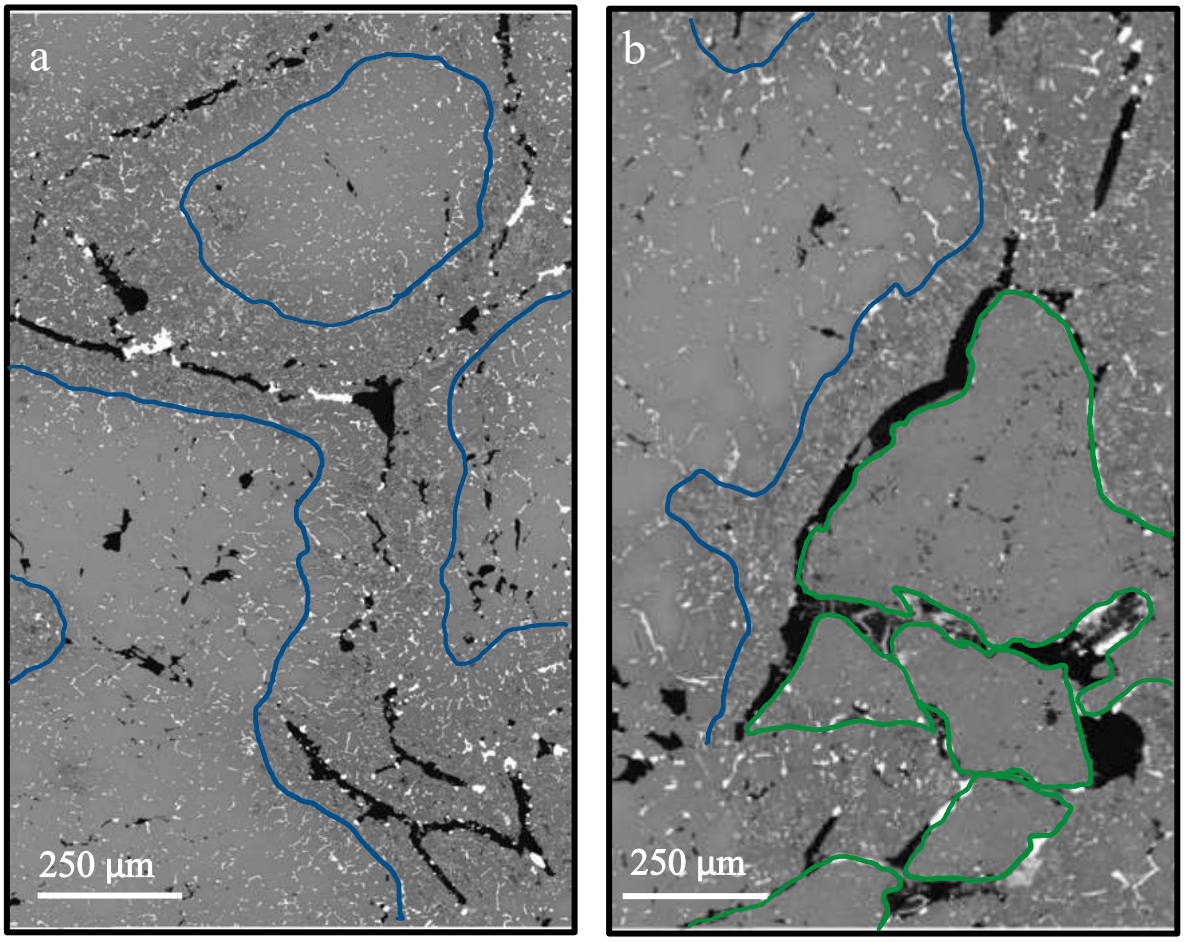

Figure 15: BSE image of the rims observed within the olivine grains of the Haverö. The green outlines the pyroxene grains with the blue representing the edge of the rims within the olivine grains, while the white represents the iron-rich metal and the black carbon. The rims present represent Mg-poor cores (light grey) and Mg-rich rims (dark grey). (a) Shows three olivine grains which meet at a triple junction that all contain rims with iron blebs visible between the boundary and within the grains themselves. (b) Presence of pyroxene grain in the centre of the image and the olivine toward to the upper left of the image with a clear outline of the boundary between the Mg-poor and Mg-rich regions of the grain.

3.1.3.2 Haverö Microstructures

BSE images of Haverö (Fig.16b) reveal that iron-rich metal is not commonly present as veins but instead occurs as small blebs across the olivine crystals. Due to the nature of the iron-rich metal within the sample, no average thickness could be calculated. Meanwhile, the carbon is present as veins (average thickness: 0.092 mm (n=14)) within the Haverö sample (Fig.16a). The average thickness of carbon in Haverö is the overall thickest of all carbon regions found across all the ureilites samples in this study. The olivine grains also contain the 120º triple junctions and signs of stage 2 shock (Fig.14a).

Haverö shows no signs of faulting, displacement or orientation of the grains. Larger fracturing between the olivine-pyroxene grain boundary (average thickness: 0.027 mm (n=8)), with the boundary thickness for the olivine-olivine grain boundary being 0.016 mm (n=8). While the olivine-pyroxene grain boundaries hold an average thickness of 0.027 mm (n=8). Haverö does show moderate levels of shock.

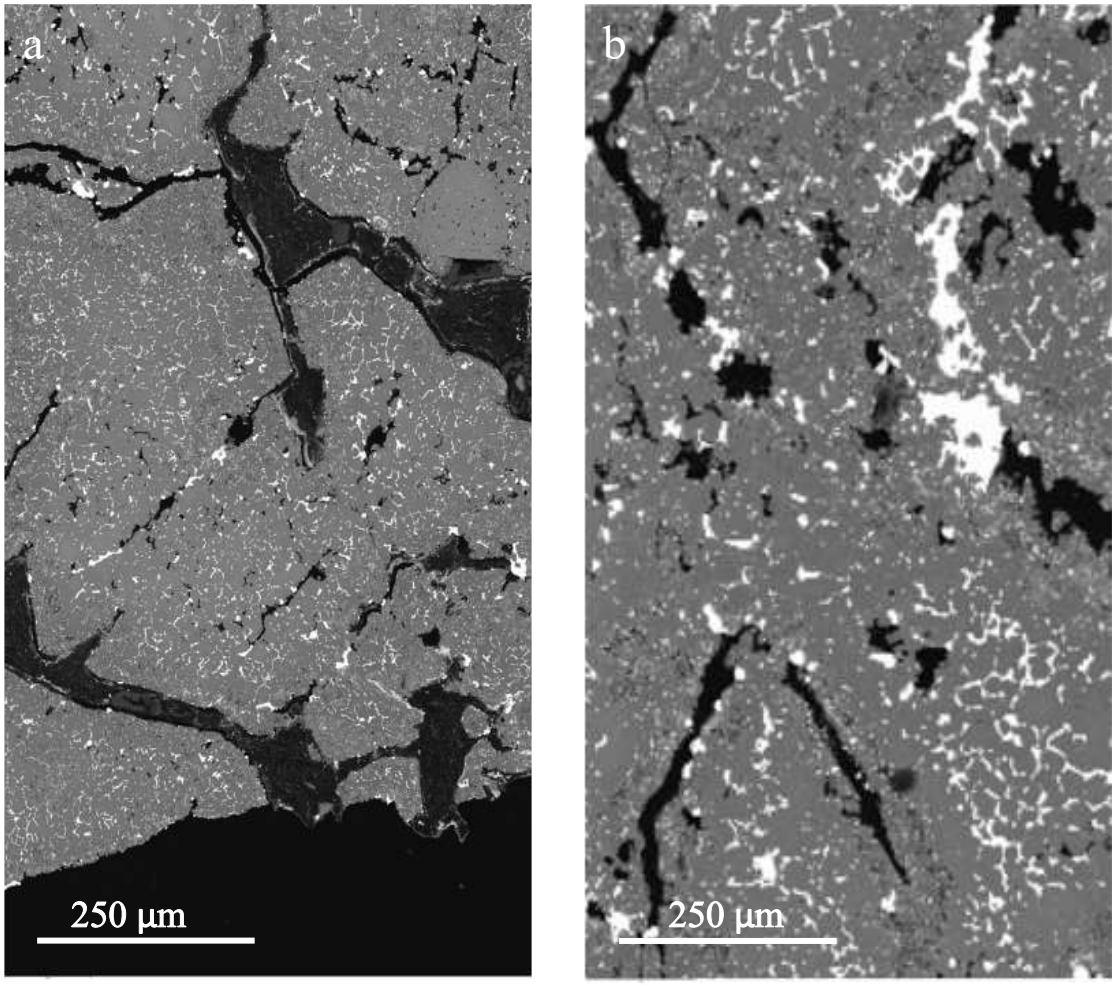

Figure 16: BSE images of carbon veining and the iron-rich metal blebs visible in Haverö. (a) Demonstrating the carbon (black) region located in the upper and lower areas of the image surrounded by olivine grains. (b) Iron-rich metal (white) infilling space as small blebs within the olivine grains as well as smaller particles of iron-rich metal in the olivine grains themselves.

3.2.1 Aubrite Petrology

The Cumberland Falls meteorite is a brecciated meteorite containing fragments of chondritic and achondritic material. The bulk wt % composition determined from an EDS sum spectrum of the whole of Cumberland Falls sample excluding the resin shows a chemical composition containing oxygen (41.6%), magnesium (20.8%), iron (15.7%) and silicon (19.5%) with minor amounts of Ca, Cr, Mn and S. The studied sample consists of three distinct sections. The three sections which for the purpose of this thesis the sample shall be spilt and referred to are the coarse breccia (Fig.17a), fine breccia (Fig.17b), and chondritic clasts (Fig.17c) respectively.

The coarse breccia section of this sample exhibits the classic brecciated texture associated with aubrites (Lipschutz et al., 1988). The section contains clear uniform sub-angular to sub-rounded shaped pyroxene grains (66%) with an average grain size of 0.8 mm. These coarser pyroxene crystals are suspended in a fine-grained pyroxene-olivine-rich matrix (34%) (Fig.17a). Iron metal blebs are also found in the coarse breccia section and are concentrated in a central area of the section. The size of these iron metal blebs ranges from 0.04 mm to 0.33 mm. Quantitative EDS measurements produced for the accuracy of one-decimal places for the coarse breccia section provided an Mg# 1.0. The ternary plot of the coarse breccia section (Fig.18) using quantitative EDS data for the section shows the following average values of Mg: 97.7% Fe: 0.9% Ca: 1.4%.

The fine brecciated section is the largest section of this sample making up two-thirds of the overall sample area (Fig.17b). The overall mineralogy of this section consists of pyroxene grains (87.39%) which are angular in shape, having a grain size of 0.4 mm (n=9) set in a fine-grained pyroxene matrix, the rest of the mineralogy consists of olivine (1.95%), iron metal (4.09%), carbon (4.26%) and chondritic material (2.31%) some of which being finer grains too small to provide accurate grain size or shape.

Within the fine brecciated section rounded iron blebs are present ranging in size from 0.64 mm to 0.084 mm (n=12) (Fig.17b). The chondritic clasts are exclusively found embedded within the fine brecciated section. The quantitative EDS Mg# values again to an accuracy of one decimal place for the pyroxene-rich matrix in the fine breccia section is 1.0 while the pyroxene-rich chondrules in the fine breccia produce an Mg# of 0.8. The ternary plot of the fine breccia section (Fig.18) shows the following average values of Mg: 86.3% Fe: 13.7%

Ca: 0.1%. Chondritic material can be observed within the matrix of the finer breccia with barred olivine pyroxene chondrules (average width 0.5 mm) to larger inclusions of chondritic material with an average width of 0.74 mm (Fig.22a).

The chondritic section has the overall mineralogy of pyroxene (54%), olivine (18%), carbon (2%), iron metal (21%) and chondrules (5%) (Fig.17c). Barred olivine-pyroxene chondrules in the chondritic section itself have an average size of 0.56 mm (Fig.22b/c), alongside iron metal blebs ranging from 0.043 mm to 0.21 mm in size. The majority of the iron metal blebs found in the Cumberland Falls sample are concentrated within the chondritic section. The quantitative EDS Mg# for the pyroxene matrix in the chondritic section is 1.0 while the olivine matrix value is 1.0 with the pyroxene-rich chondrules having a value of 1.0. The ternary plot of the chondritic section (Fig.18) shows the following average values of Mg: 75.5% Fe: 13.5% Ca: 11%

Quantitative EDS analysis for Cumberland Falls overall shows it holds a high percentage of pyroxene (88%) with lesser amounts of olivine (11%) throughout the sample across all regions, with a total average Mg# for pyroxene in the coarse breccia is 1.0, fine breccia matrix 1.0, chondrules in the fine breccia 0.8, chondritic section matrix 0.8 and finally for the chondrules 0.9 (Table 4). The Mg# for olivine present in the chondritic section matrix is 0.9 (Table 4). When the Cumberland Falls sample is plotted on a ternary plot of Fe, Mg and Ca shows that the sample contains high amounts of Mg falling in the range of 100-70% with Fe making up 10-20% and Ca averaging around 40% (Fig.18).

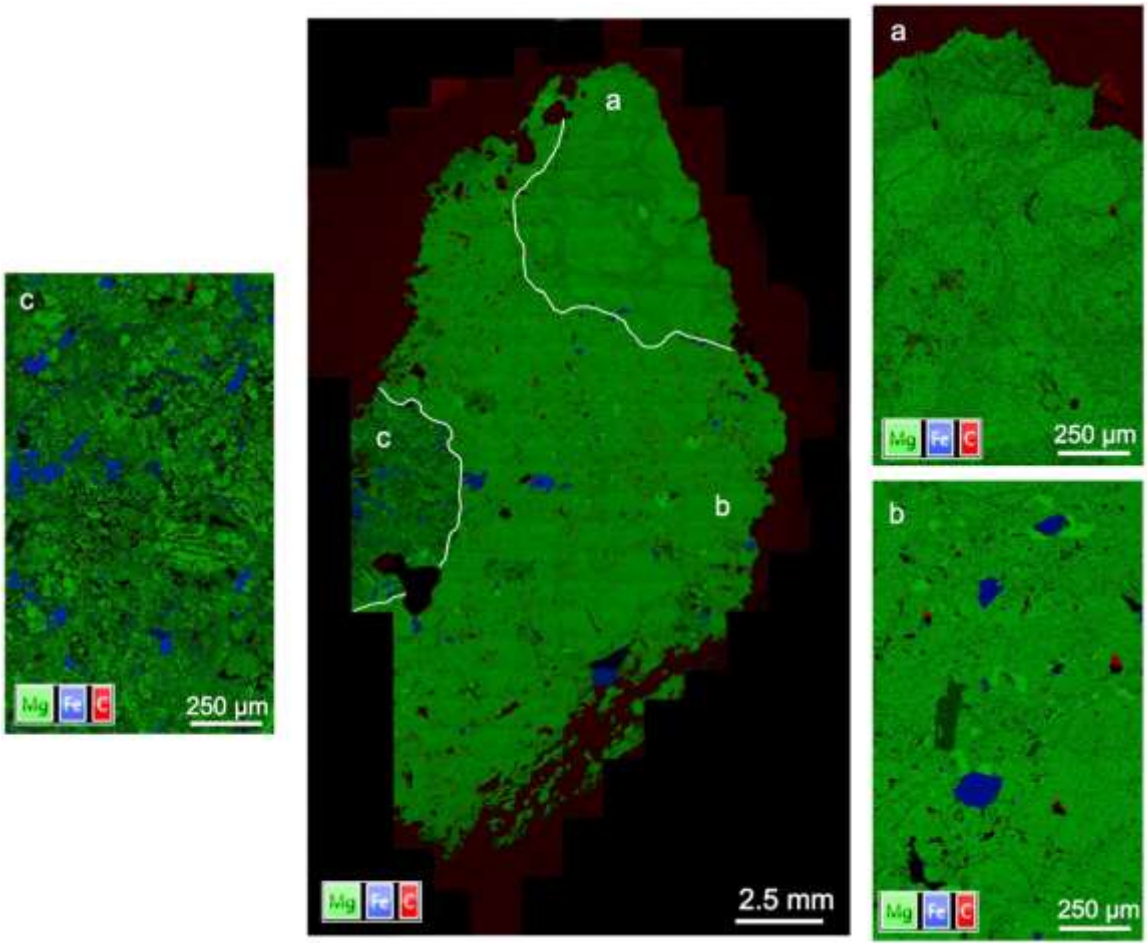

Figure 17: False coloured EDS layer montaged image map of the bulk composition for Cumberland Falls (Red: Carbon, Green: Magnesium, Blue: Iron). The white outlined areas represent the boundaries between the different textures present. These areas a, b and c are presented in close-up images of each section in more detail. (a) False colour EDS layered montaged image (Red: Carbon; Green: Magnesium; Blue: Iron) of the coarse breccia section with coarse pyroxene grains in a finer olivine-pyroxene matrix. (b) False colour EDS layer montage image (Red: Carbon; Green: Magnesium; Blue: Iron) of the fine breccia section with finer pyroxene grains in a pyroxene matrix along with the conclusion of iron-rich metal blebs and chondrules. (c) False colour EDS layer montage image (Red: Carbon; Green: Magnesium; Blue: Iron) of the chondritic section with a pyroxene-olivine matrix, iron-rich blebs and inclusion on barred olivine-pyroxene chondrules.

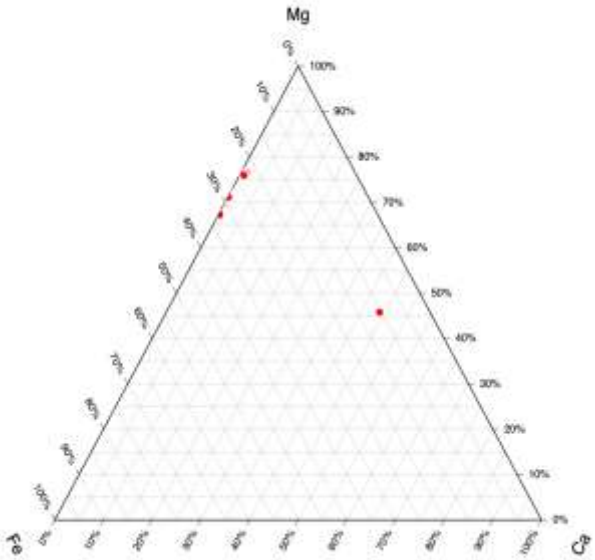

MIL 090356

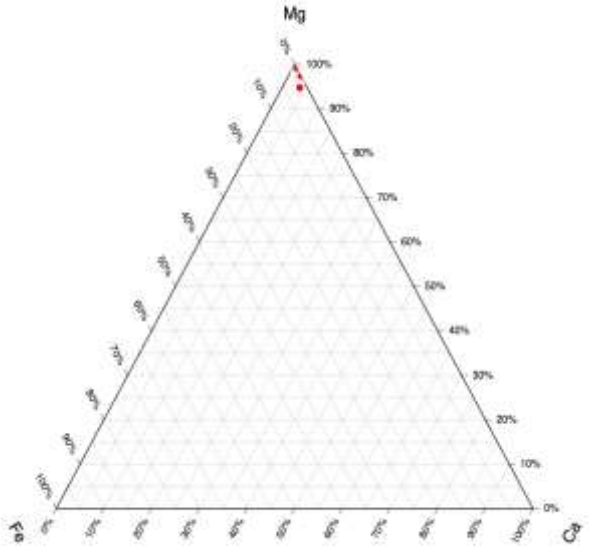

Coarse breccia

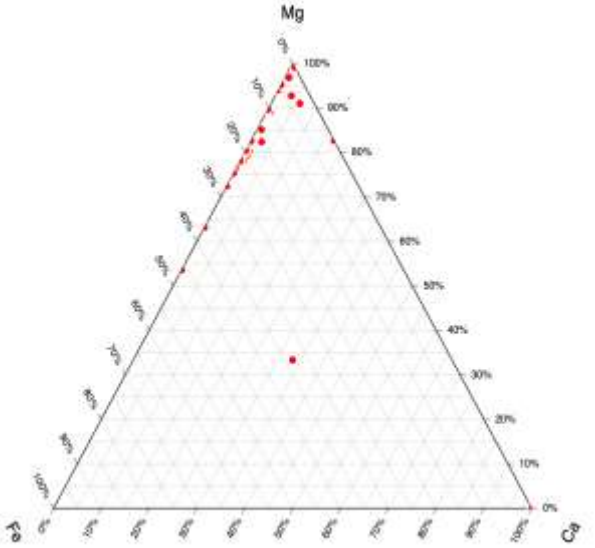

Fine breccia

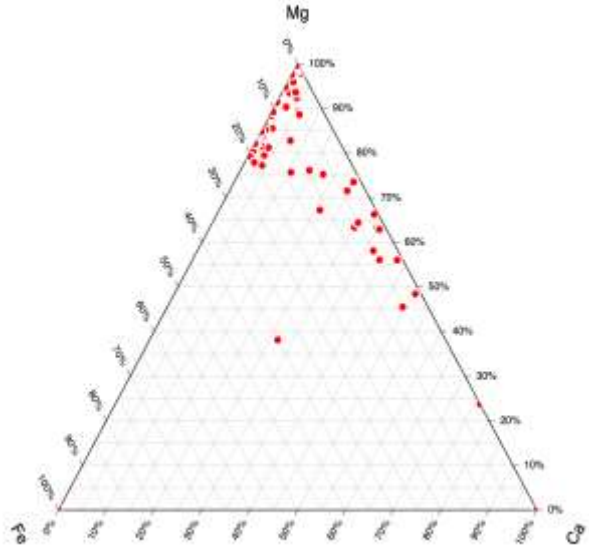

Chondrite section

Figure 18: Ternary plots of MIL 090356 and each section of the Cumberland Falls sample (coarse breccia, fine breccia, and chondritic sections) demonstrating the percentage of Mg, Fe and Ca within each of the samples.

Table 4: Mg# for each of the three sections present within Cumberland Falls focusing on the Mg# for the pyroxene, olivine and chondrules present within the sample.

Section	Pyroxene Mg#	Olivine Mg#	Barred olivine-pyroxene chondrules Mg#
Coarse Breccia	1.0 (n=9)	-	-
Fine Breccia	1.0 (n=9)	-	0.8 (n=20)
Chondritic	0.9 (n=53)	1.0 (n=15)	0.9 (n=4)

3.2.2 Aubrite Microstructures

Microstructures in the Cumberland Falls sample are uniform across all three sections. The first notable feature is that all the boundaries between each section are sharp (Fig.19). Another feature found within the larger grains of the coarse breccia, fine breccia and chondritic sections is a set of fracturing in both a horizontal and vertical direction with no displacement of the grains or the sections.

Each section shows different features. In the coarse breccia section, the most notable feature apart from the brecciated texture is the horizontal and vertical fractures present within the pyroxene grains. A larger fracture cutting across the centre of the section (Fig.20), could be a product of sample preparation, due to the lack of apparent displacement or alteration of the grains and those grains surrounding this fracture. No additional signs of shock or a shock event occur in the breccia texture.

Microstructural features found within the fine brecciated section of the Cumberland Falls sample are that the pyroxene grains also contain fractures which appear again in a horizontal and vertical direction (Fig.21a), there is also fracturing within the iron blebs (Fig.21b) in the bottom half of the section. The section has already been noted to have a sharp boundary with both the coarse brecciated section and chondritic sections. The fine breccia also contains barred olivine-pyroxene chondrules within the matrix (Fig.22a) located in the lower left of

the section within the sample. There are no signs of faulting or displacement of any of the grains or parts of the section.

The chondritic section consists of vertical fractures found in the pyroxene grains (Fig.23) throughout the section, however, there is no other faulting or displacement of the grains in the section present. Chondrules are present on the right-hand side of the section (Fig.22b/22c), near the sharp boundary between the chondritic and fine breccia sections (Fig.19).

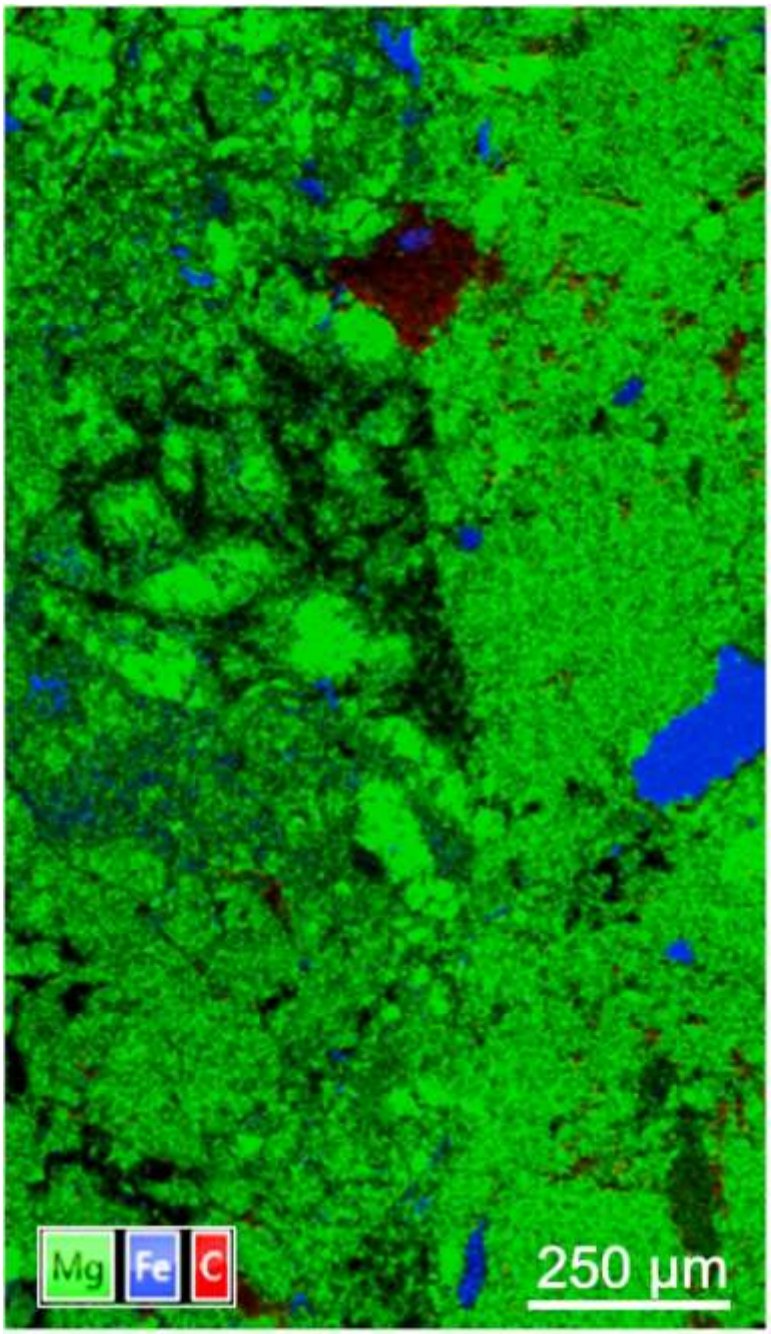

Figure 19: False colour EDS image (Red: Carbon; Green: Magnesium; Blue: Iron) of the sharp boundary between the chondritic (left) and fine breccia section (right). The boundary shows the chemical differences between the pyroxene matrix fine breccia and the pyroxene-olivine matrix of the chondritic section.

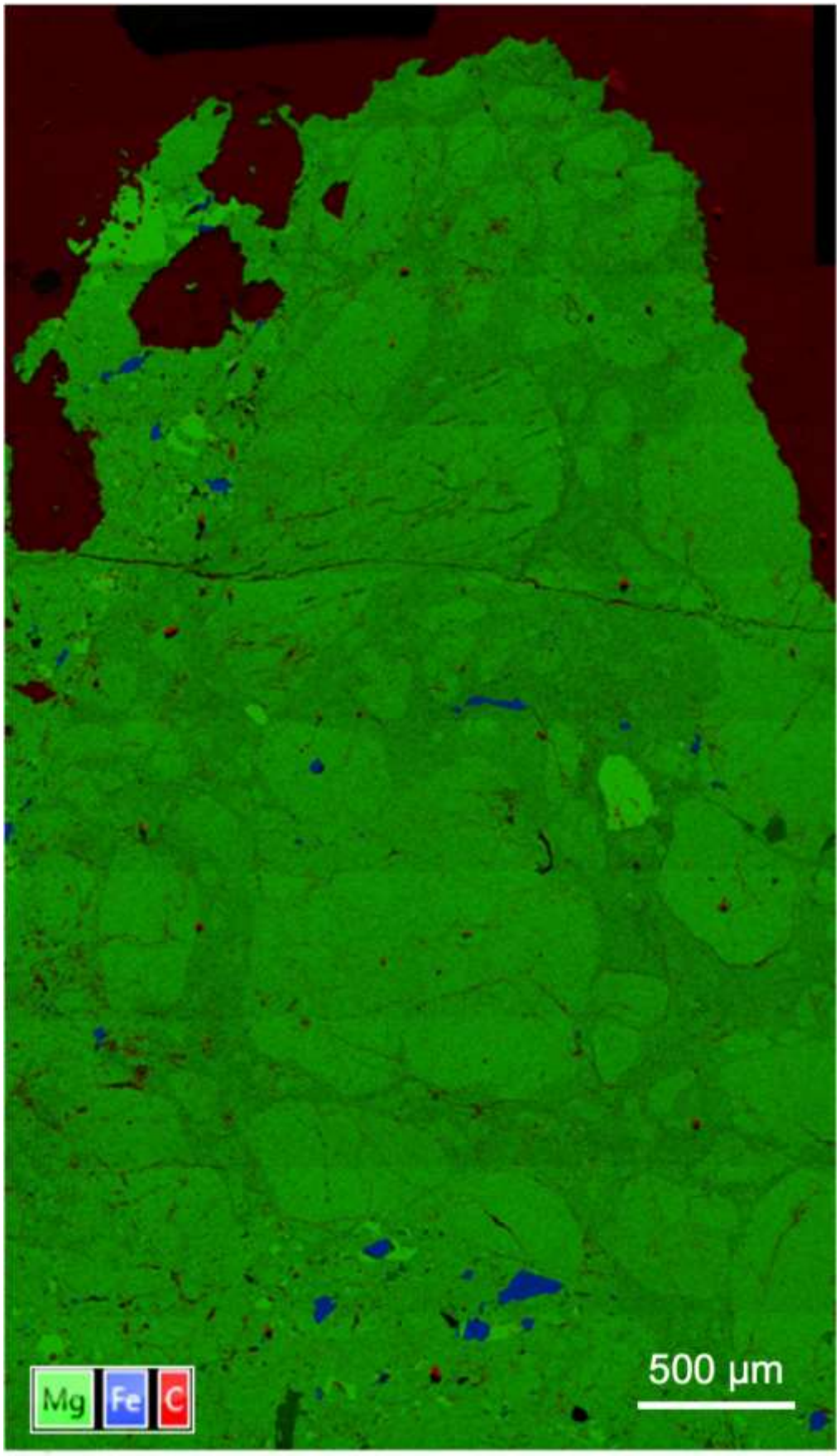

Figure 20: BSE image of the fracturing present within the coarse breccia section of Cumberland Falls with the sharp boundary to the fine breccia section present at the base of the image, fracturing of the pyroxene grains at the base of the section as well as toward the upper centre of the section with the fractures appearing as both horizontal and vertical, with the fracture cutting through the section itself, most likely as a result of sample prep.

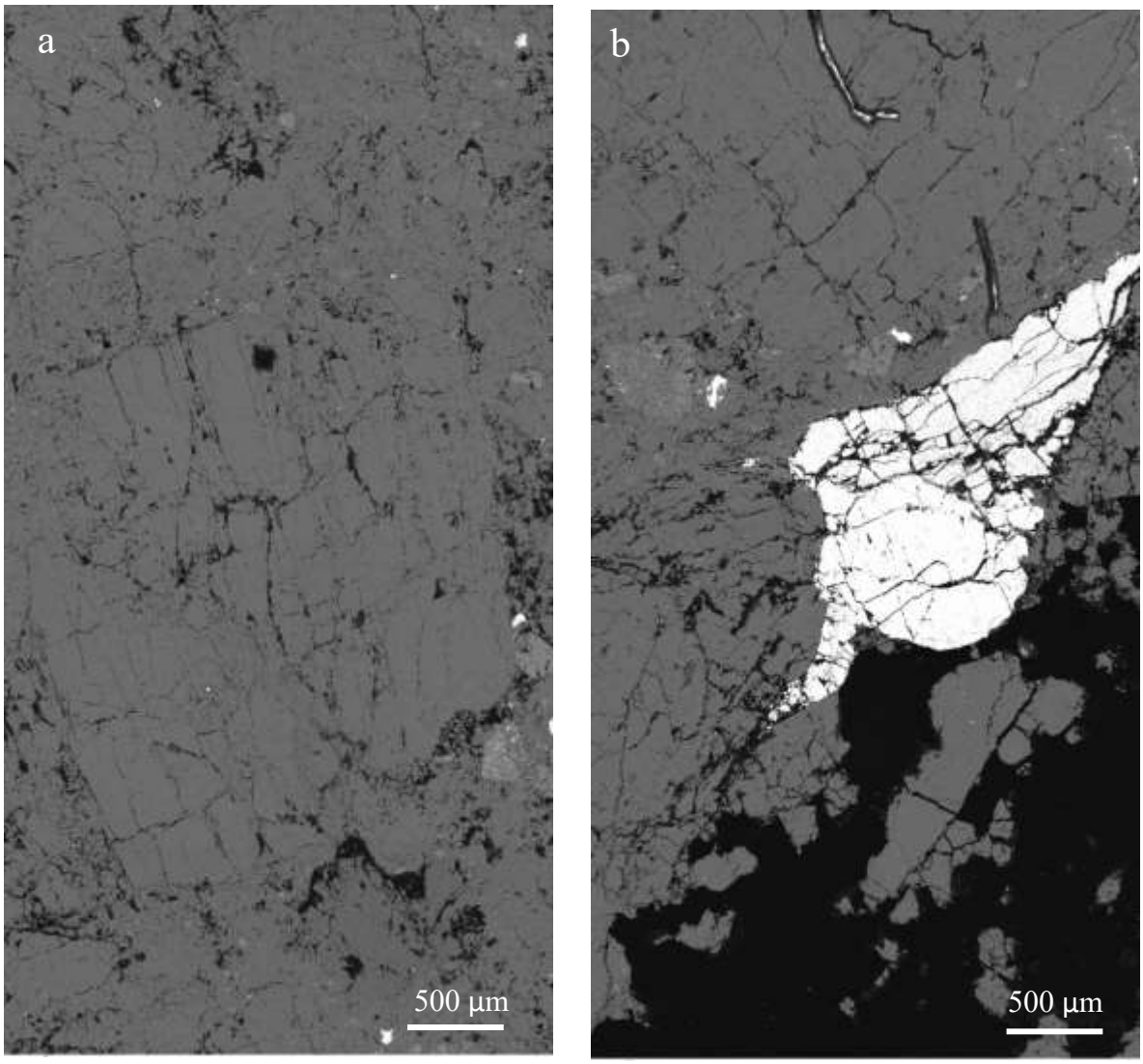

Figure 21: BSE image of the vertical and horizontal fractures present within Cumberland Falls fine breccia and chondritic sections. (a) Horizontal and vertical fracturing within the large pyroxene grain within the chondritic section (b) Fracturing within the iron bleb (white) located at the bottom of the fine breccia section within Cumberland Falls, within fracturing present in the surrounding pyroxene grains.

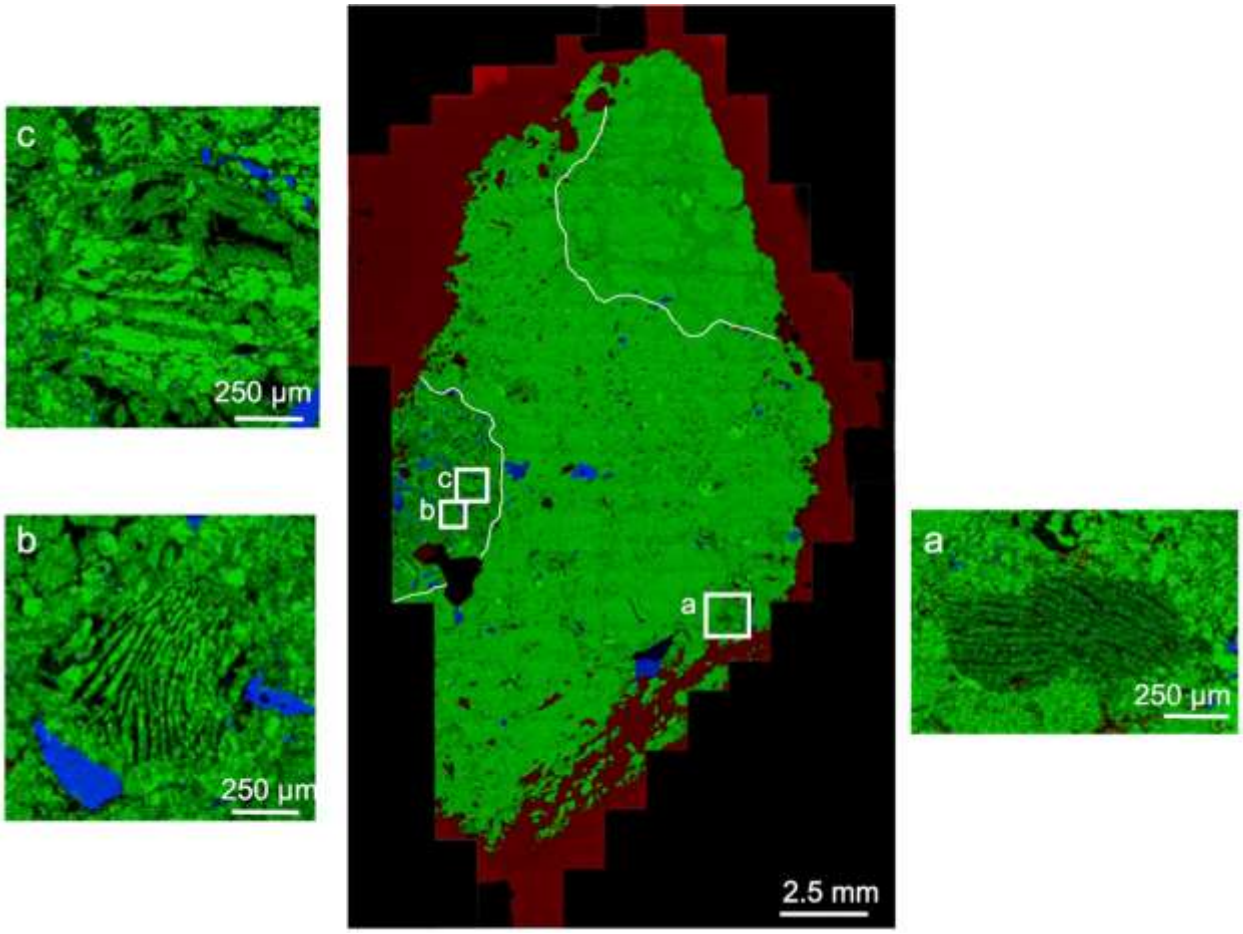

Figure 22: False colour EDS image of Cumberland Falls (Red: Carbon; Green: Magnesium; Blue: Iron) with the white lines outlining the separate textural sections observed in the sample. The white boxes show the close-up images of the barred olivine-pyroxene chondrules (Light green: Olivine; Dark green: Pyroxene) present across the sample within the fine brecciated and chondritic sections.

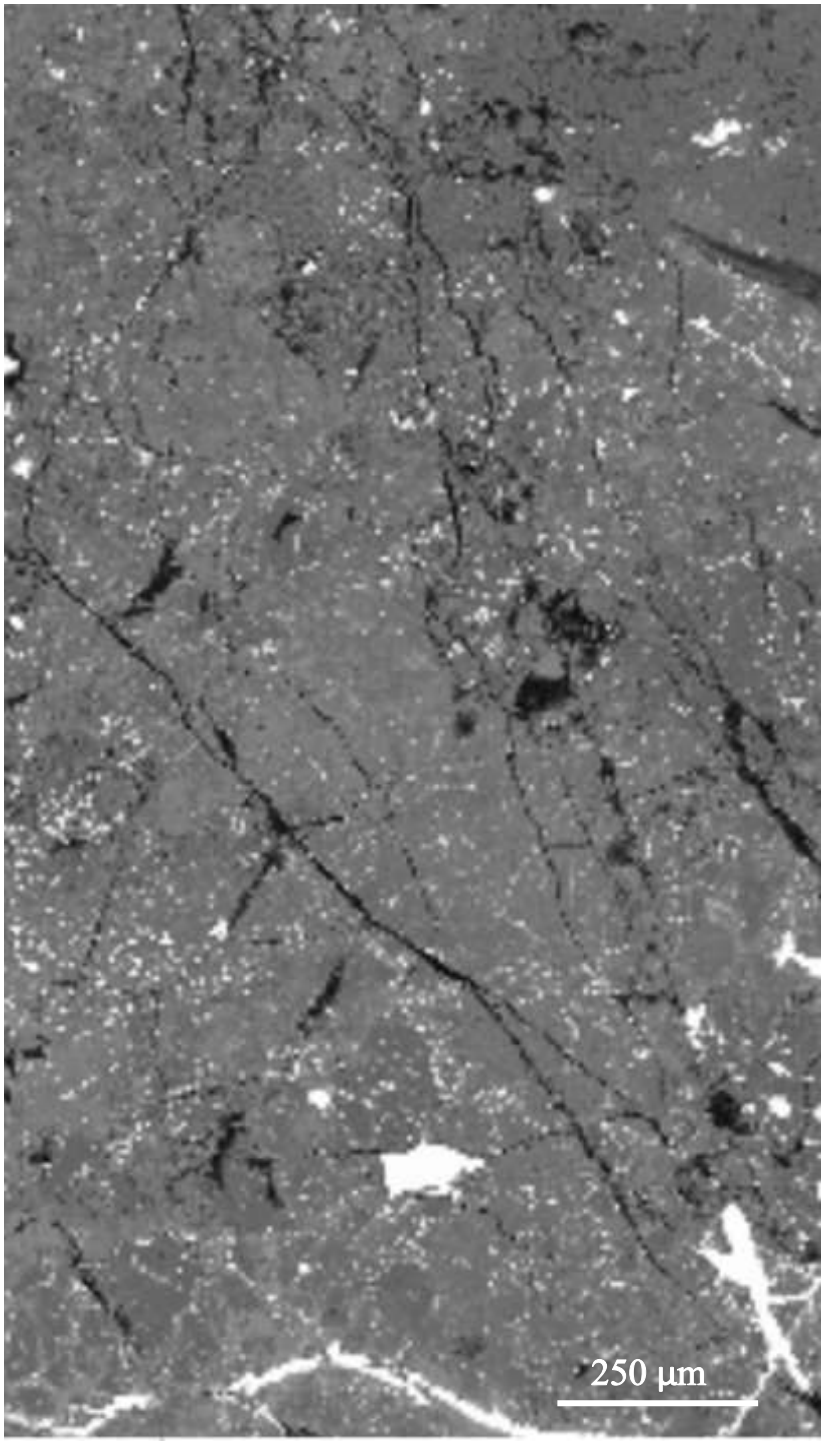

Figure 23: BSE image of the chondritic section in Cumberland Falls demonstrating the presence of fracturing within the grains and matrix of this section, however, no signs of faulting or displacement are visible.

3.3.1 Anomalous Achondrite Petrology

The wt% composition for MIL 090356 shows the chemical composition to consist of oxygen (35.7%), iron (24.3%), magnesium (19%) and silicon (16.3%) with minor amounts of Cl, S, Cr, Ca, Mn and Ni. While the overall area % for the bulk composition is olivine (64%), pyroxene (3%), iron metal (32%) and carbon (1%). This can be compared to the bulk composition of the ureilite sample in Table 5 allowing for a comparison of all the samples, to see the similarities and differences due to the original misclassification of MIL 090356.

EDS false colour map (Fig.24c) for MIL 090356 shows the distribution of olivine and pyroxene within the sample with the BSE image showing the presents of iron-rich metal in the form of veining throughout the sample (Fig.24a). The olivine grains appear uniform with a sub-rounded shape, triple junction boundaries of 120º (Fig.24b) an average grain size of 0.24 mm while the pyroxene grains have a grain size of 0.36 mm, with no triple junction boundaries and a more sub-angular appearance to their shape. Within MIL 090356 there is no matrix, but there is the presence of iron-rich metal veining between the grains, similar to that of the ureilites.

EMPA data for MIL 090356 produced a ternary plot of olivine (Fig.18) that shows the following average relative abundance values of Mg: 73.4% Fe: 26.5% Ca: 0.1% in the sample indicating a lack of Ca within the sample but a high abundance of Mg (~70%) and Fe (~30%). The Mg# for the sample was also produced with the result showing that for olivine an Mg# of 0.7 (n=9). .

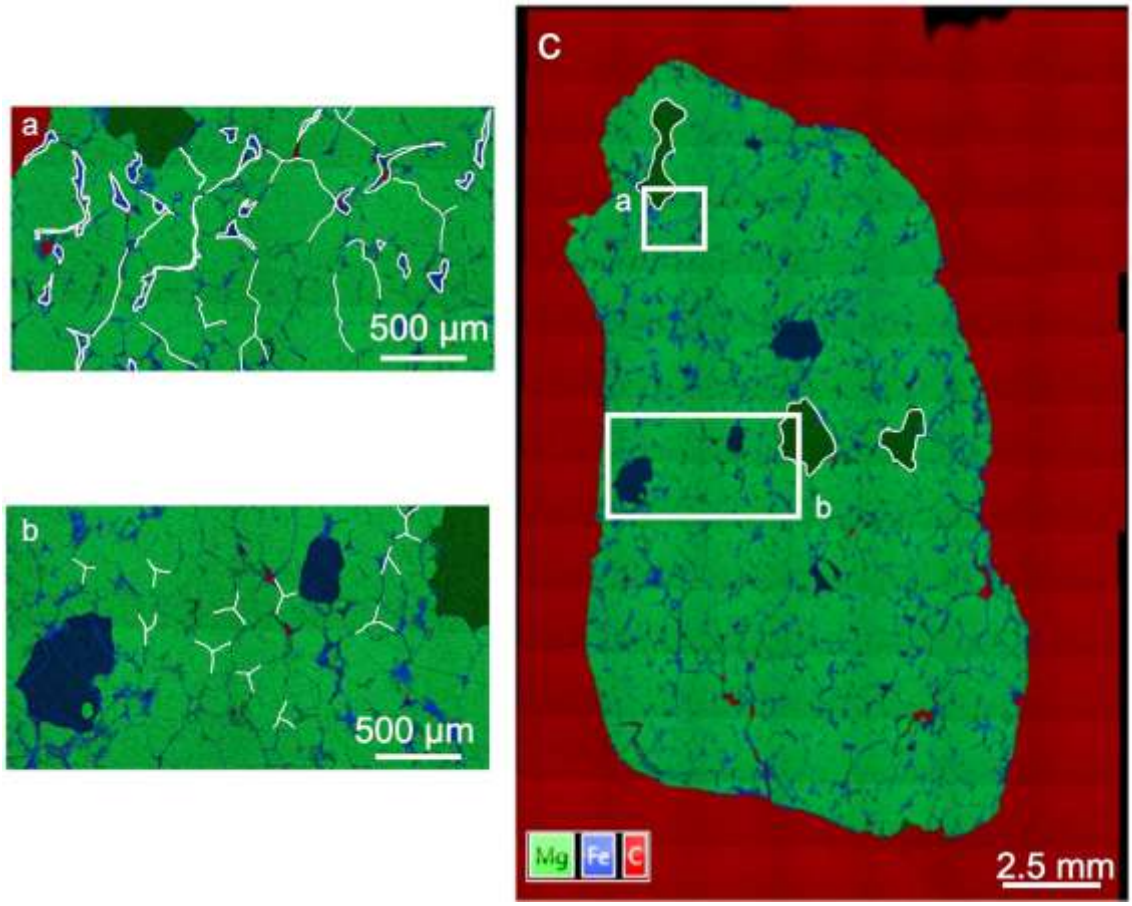

Figure 24: (a) False colour EDS image (Red: Carbon; Green: Magnesium; Blue: Iron) of the iron veining (outlined in white) present in MIL 090356. The veining is spread equally across the sample. (b) False colour EDS image (Red: Carbon; Green: Magnesium; Blue: Iron) of some of the triple junctions present in the olivine grains (outlined in white) within the sample. (c) False coloured EDS layer montaged image map of the bulk composition for MIL 090356 (Red: Carbon, Green: Magnesium, Blue: Iron). The white outlined areas represent the pyroxene grains which are of a darker green compared to that of olivine with the white boxes a and b representing the close-up areas of the iron and triple junctions (120º) present in the sample. The iron-rich metal appears as veins infilling fractures in the grain boundaries, with carbon present most likely in the form of graphite and/or diamond.

3.3.2 Anomalous Achondrite Microstructures

The iron veining found within the MIL 090356 is relatively consistent throughout the sample compared to that found across the ureilite samples infilling the grain boundaries throughout the sample, with an average thickness of the veins being 0.006 mm across the sample. As

well as MIL 090356 not showing any evidence of fractures, faults, displacement or orientation of the grains in the sample.

EBSD GROD angle and KAM maps of MIL 090356 show a general lack of deformation throughout the section with the GROD angle map having an average internal misorientation of 0-3°. Deformation present is concentrated around the central area of the section where internal misorientation increases to 6º degrees (Fig.25a). The KAM map shows an average misorientation of 0-2° this lack of deformation and misorientation of the grains matches the uniform appearance of the sample and overall lack of fracturing witnessed apart from the upper right corner of the sample (Fig.25b), the Grain Orientation Spread (GOS) and Mean Orientation Spread (MOS) for the olivine grains in MIL 090356 show that GOS is 12.2º and the MOS is 0.7º. One point per grain pole figures for olivine (Fig.26) show that the <100> <010> <001> axes all have point clusters that are orthogonal to each other, consistent with a lineation fabric. The crystal rotation axes diagram shows a strong concentration of points consistent with deformation being accommodated by rotation around the <100> <010> planes.

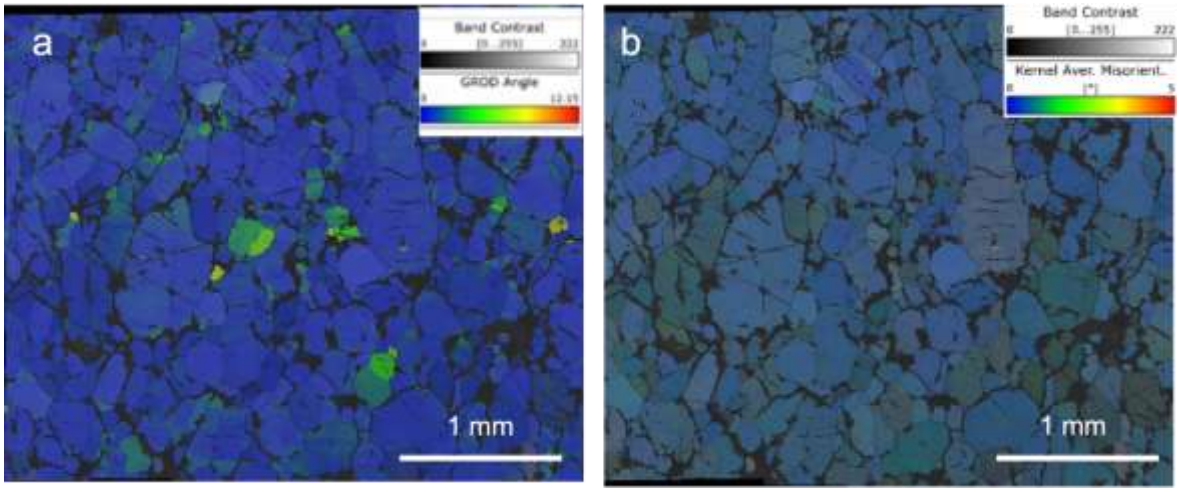

Figure 25: (a) GROD angle map taken from the middle section of the MIL 090356 sample with undeformed crystals in blue, those that see increased internal deformation are highlighted through the progression of colours to green. The maximum amount of internal deformation is located mainly in the centre of the map with a deformation of 6°. (b) KAM map from the same section of MIL 090356, the highest amounts of misorientation is up to 2º with the misorientation concentrated to the lower half of the map.

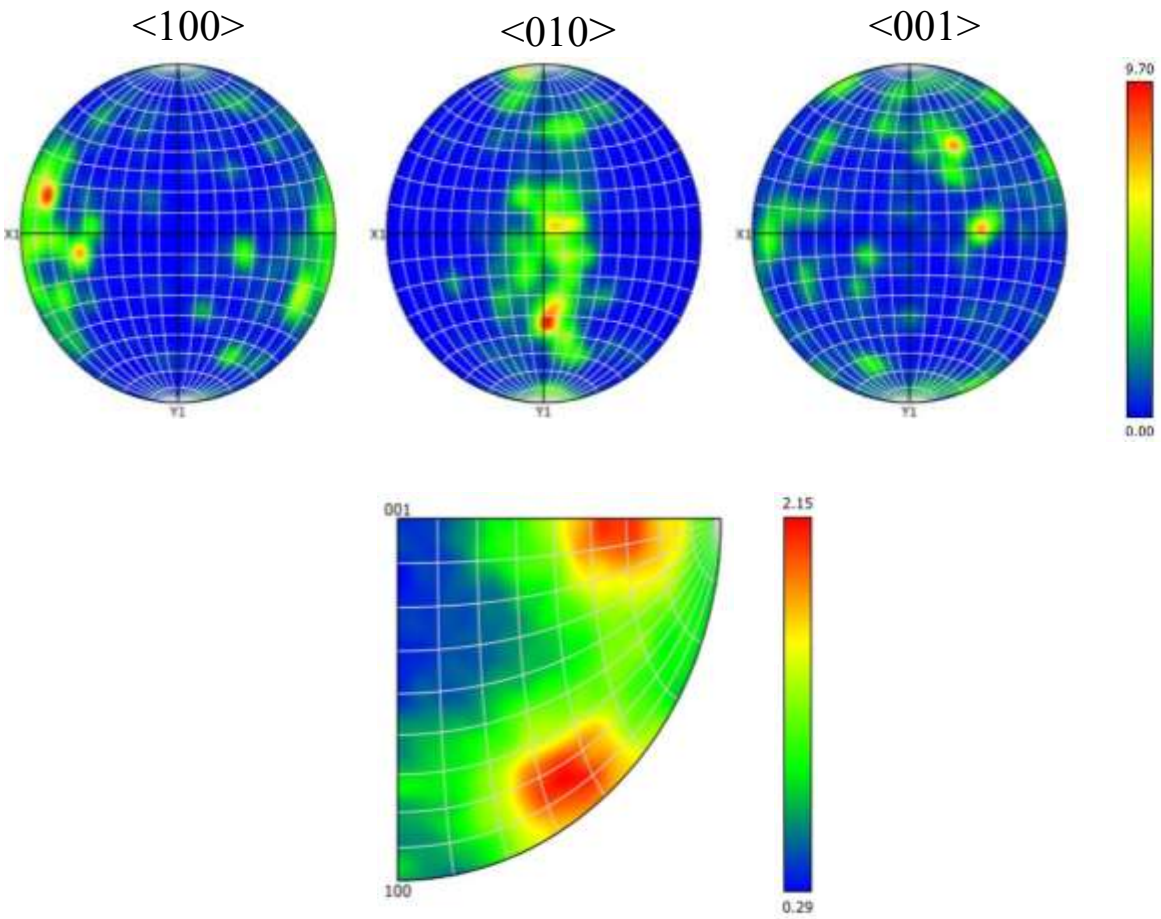

Figure 26: Top: pole figure at one point per grain for the orientation of olivine grains within MIL 090356 collected using EBSD data. The grains show a strong alinement along the <010> and <100> planes matching that of the Euler map. Pole figures of olivine in MIL 090356. Bottom: Crystal rotation axes inverse crystal coordination pole figure showing a cluster along the <100> and <010> axis.

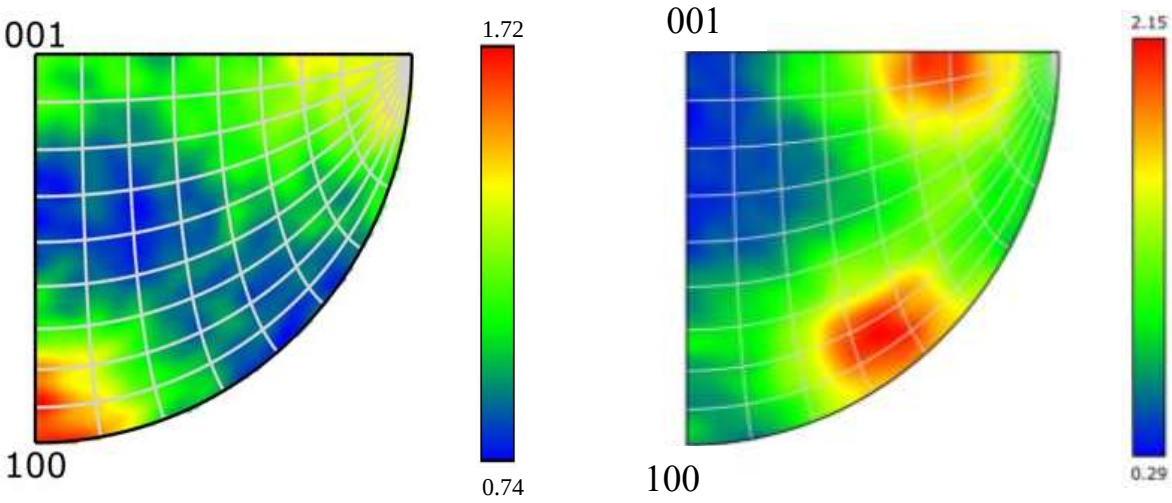

Figure 27: Crystallographic rotation axes for Reid 016 (left) which shows a cluster around the <100> axis and MIL 090356 (right) showing a cluster in the hk0 [c] section and along the <010> axis.

Table 5: The relative area bulk percentage abundance of olivine, pyroxene, iron-rich metal and carbon within the ureilites; Reid 016, Nova 001 and Haverö and anomalous achondrite MIL 090356.

Sample	Olivine (%)	Pyroxene (%)	Iron-rich metal	Carbon
Reid 016	66	12	17	5
Nova 001	56	24	10	10
Haverö	80	6	2	12
MIL 090356	64	3	32	1

4. Discussion

In this thesis, the petrology and microstructures of three different achondrite groups have been studied. The achondrite groups and specific meteorites studied were the ureilites Reid 016, Nova 001 and Haverö; the aubrite Cumberland Falls and an anomalous achondrite MIL 090356. The bulk petrology and mineralogy (Table 6) of all achondrite samples measured here are generally consistent with the literature. However, there are subtle textural variations both within and between the studied achondrites i.e., variable reaction rim thicknesses and metal abundance within ureilites; textural similarities between ureilites and the anomalous achondrite MIL 090356; and the classification of the chondritic clasts in the Cumberland Falls aubrite. These petrological variations will be presented in this discussion and the implications for their achondrite parent body discussed.

Table 6: Comparison of the bulk chemical composition and mineralogy of all samples studied within the thesis.

Sample	wt% bulk composition	Minerology
Reid 016	Oxygen (38.6%) Magnesium (21.6%) Iron (17.9%) Silicon (17.9%) Minor amounts of Cr, Mn, S, Ni and Al	Olivine (66%) Clinopyroxene (12%) Iron metal (17%) Carbon (5%)
Nova 001	Oxygen (41.6%) Magnesium (20.8%) Iron (15.7%) Silicon (19.5%) Minor amounts of Cr, Mn, S and Ca	Olivine (56%) Pyroxene (24%) Iron metal (10%) Carbon (10%)
Haverö	Oxygen (41.8%) Magnesium (24.8%) Iron (13.7%) Silicon (18.5%) Minor amounts of Cr, Mn and Ca	Olivine (80%) Pyroxene (6%) Iron metal (2%) Carbon (12%)
MIL 090356	Oxygen (35.7%) Magnesium (19%) Iron (24.3%) Silicon (16.3%) Minor amounts of Cr, Mn, S, Ni, Ca and Cl	Olivine (64%) Pyroxene (3%) Iron metal (32%) Carbon (1%).
Cumberland Falls	Oxygen (41.6%) Magnesium (20.8%) Iron (15.7%) Silicon (19.5%) Minor amounts of Cr, Mn, S and Ca	Olivine (12%) Pyroxene (82%) Iron metal (4%) Carbon (2%) Chondrules (1%)

4.1 Ureilites

The reaction rims, carbon content and associated nanodiamonds of the ureilites are interpreted as either 1) the product of the slow cooling of a carbon-rich ultramafic rock in a mantle or plutonic setting (Nabiei et al., 2018), or 2) impact injection of carbon-rich material during an impact with a carbonaceous chondrite asteroid (Nabiei et al., 2018). If the carbon content and reaction rim textures are produced by slow cooling in a pluton or mantle setting, we would expect to observe equilibrium textures (Rubin, 2006). If impact injection of carbon-rich material we would expect to observe disequilibrium textures that may vary between samples either due to proximity to the impactor or different impacts on discrete UPBs (Rubin, 2006).

The major minerals in the ureilites studied are on average 67 area% of olivine with an average grain size of 0.66 mm and 14 area% of pyroxene with an average grain size of 0.47 mm. The olivine abundance varies by 20 area % across the ureilites and pyroxene varies by 10 % between the ureilites. The major silicate mineral abundances and textures are consistent with literature descriptions (Downes, 2008; McSween, 1987). Olivine grains form 120º triple junctions (Fig. 6a, 11a, 14a) which suggest an equilibrium cumulate texture, matching literature descriptions (Downes, 2008) and is consistent with slow cooling in a cumulate plutonic or mantle environment. The silicate grains were fractured in all samples (Fig. 6a, 11a, 14a) as such consistent with shock stage 2 in alignment with the literature descriptions of ureilites, suggesting shock pressures of ~1-5 GPa and post-shock temperatures of ~0 °C (Stöffler et al., 2018; Rubin, 2010).

The olivine grains in Reid 016 have a moderate crystallographic preferred orientation, while there is a weak crystallographic preferred orientation observed within Haverö, and no preferred alignment is observed in Nova 001. Similar textures described in the literature show that they are mineral lineations (Treiman and Berkley, 1994; Wlotzka, 1972). These lineations can be formed by the flow and settling of the minerals in a plutonic or mantle environment (Berkley et al., 1980). This lineation texture suggests that Reid 016 and to a lesser extent Haverö experienced some flow component within the pluton/mantle evidencing silicate textural equilibrium in the ureilites (Grossman, 1998; Neuvonen et al., 1972). Nova 001 shows no mineral alignment. This could be caused by 1) no external stress field acted on Nova 001 during and/or after crystallisation; or 2) a cutting artefact where the plane of the section is perpendicular to the mineral lineation during sample preparation, causing

lineation not to be observable on a 2D sample surface. 3D textural analysis using XCT (X-ray Computed Tomography) supplemented with further EBSD would be required to determine if Nova 001 does have a random fabric or not. If all samples do have a mineral lineation this suggests that there is deformation occurring across the whole planetary body, whereas, if samples have various textures this suggests that separate pluton/mantle systems across the parent body result in different texture formations.

CRA diagrams of olivine in Reid 016 (Fig.29) show a cluster at the <100> axis which is consistent with low temperatures of <600 ºC deformation (Ruzicka and Hugo., 2018) on the ureilite parent body (UPB). This deformation could have occurred before during or after the redox reaction. It is unlikely that this low-temperature deformation occurred prior to the redox reaction because the cumulate textures and 120° triple junctions of olivine suggest annealing at mantle-plutonic temperatures. As will be discussed redox reaction conditions require temperatures of 1126 – 726 ºC (Langendam et al., 2021) that are also inconsistent with the inferred deformation temperatures from CRA. As such it is unlikely that this deformation occurred during redox reactions. The most likely explanation is that this low temperature deformation was caused by a later impact event that postdates the redox reaction, ejecting the sample from the UPB.

The ureilites iron metal content, carbon content, reaction rim thickness and vein thickness vary between samples. The bulk iron metal content of the ureilites (Fig.28) varies from 2% in Haverö, through 10% for Nova 001 up to 17% for Reid 016. The bulk carbon content of the ureilites (Fig. 28) varies from 5% in Reid 016 through 10% Nova 001 up to 12% for Haverö (Figure 28, Table 5). Iron metal veining was also observed in Reid 016 and Nova 001. The thickness of these metal veins varies from 0.015 mm for Nova 001 and up to 0.018 mm for Reid 016, with Haverö containing iron particles along the olivine grain boundary forming the beginnings of the iron veining observed in the other ureilite samples. Carbon-rich veining is also observed across the ureilites and varies from 0.036 mm in Nova 001 to 0.068 mm in Reid 016 and up to 0.092 mm for Haverö. Another feature seen in all the samples is the presence of reduction rims of the olivine grains producing Mg-poor cores and Mg-rich rims. The Mg-rich olivine rims also contain iron metal particles. The core rim structure of these textures suggests that the reduction reaction did not reach completion, leaving samples in disequilibrium (Rubin, 2006). These reduction rims have a range of thicknesses from 0.085 mm for Nova 001 to 0.116 mm in Haverö and up to 0.15 mm in Reid 016.

Comparing reduction rims thicknesses to the iron and carbon content. Reid 016 has the highest iron (17%) and lowest carbon (5%) content with the thickest reduction rims (average = 0.15 mm); followed by Nova 001 with an iron metal content 10%, a carbon content of 10% and reduction rim average thickness of 0.085 mm, finally; Haverö has an iron metal content of 2%, a carbon content of 12% and reduction rim average thickness of 0.116 mm. Based on the observed iron and carbon contents and Reid 016 containing the thickest reduction rims it would be expected that Haverö to have the thinnest veins, not Nova 001, forming a pattern in reduction rim thickness based on the extent to which the redox reaction took place. Thicker rims in Haverö can be explained by the recrystallisation of the sample causing a thicker reduction rim after the initial reaction took place (Vdoykin, 1976).

The reduction rims form via a redox reaction with C-rich material defined by the following equation (Langendam et al., 2021).

$$C + FeMgSiO_4 = MgSiO_3 + Fe + CO_{(g)}$$

The pressure-temperature conditions required for the progression of this redox reaction are pressures of <10 MPa and temperatures of 1126 – 726 ºC (Langendam et al., 2021; Wasson et al., 1976). Miyamoto et al. (1985) showed the cooling rate for samples studied being of a short time period ranging from 2-6 ºC/hour with each sample having its own specific cooling rate within this zone. The calculation for this reaction is based on the reverse zoning profile of Fa components at the grain boundary of the olivine. These differences in cooling rate between samples can explain the differences in reduction rim thicknesses across the samples, based on the samples being exposed to the correct reaction conditions for varying amounts of time. Reid 016 with the thickest reduction rims of 0.15 mm experienced the longest period of cooling followed by Haverö at 0.116 mm and Nova 001 with a reduction rim thickness of 0.085 mm experiencing the shortest cooling period of the samples in the study.

Using the reduction rim thickness and residual carbon as a proxy for the extent of the redox reaction suggests that Reid 016 experienced redox reaction conditions to the greatest extent with the majority of carbon going through the reaction to produce the iron veining and thickest reduction rims with Mg-depleted olivine and Fe-metal particles. Nova 001's equal carbon and iron metal abundance could be interpreted as the midpoint in the reaction where half the carbon has been consumed. The high carbon low metal content of Haverö can therefore be interpreted as this sample having experienced redox reaction conditions for the

shortest time. However, the reduction rims of Nova 001 are thinner than Haverö which suggests that the progress of the redox reaction does not solely control the reduction rim thickness.

The olivine cumulate texture and 120° triple junctions are consistent with equilibrium textures and suggest the sample was initially formed at depth either in a pluton or mantle environment with some component of flow. However, the reduction rims represent disequilibrium textures and are inconsistent with slow cooling in a mantle or plutonic environment where the temperatures would allow the reaction to reach completion. The reduction rims coupled with the iron metal and carbon veining, suggest that the reduction rims were most likely produced by an impact event. Barrat et al. (2017) have suggested that the UPB contained carbon originally with volatile-rich material different from that known in carbonaceous chondrites and was present in some areas of the early Solar System and present in at least one large rocky protoplanet. Studies of the C and O isotopic compositions indicate that the chemistry of the ureilitic mantle has recorded the involvement of two C-rich reservoirs characterised by distinct $\delta^{13}C$, $\delta^{18}O$, ^{17}O and Fe/Mg ratios (Barrat et al., 2017). Suggesting that carbon was present on the UPB, but a possible later impact event introduced a second C-rich reservoir and caused the disequilibrium textures observed.

In this instance the scenario varies in redox conditions that could be explained by 1) multiple impactors with different carbon contents and potentially on different parent bodies, or 2) proximity to the impactor resulting in prolonged redox conditions or more being injected. The extent to which a single scenario can be defined based on the data collected cannot be concluded; EBSD analysis of Haverö and Nova 001 is required as well as heterogeneous oxygen isotope data to identify single or multiple impactors, since no good candidate for the UPB has yet been discovered (Goodrich et al., 2017). The implications of scenario 1) multiple impact events on potentially more than one parent body are such that the availability of carbonaceous impact material in the Solar System, but also increases chances of identifying a UPB candidate. If scenario 2) a single event on a singular UPB would likely result in lower amounts of carbonaceous impact material available within the region and thus lower odds of identifying a UPB.

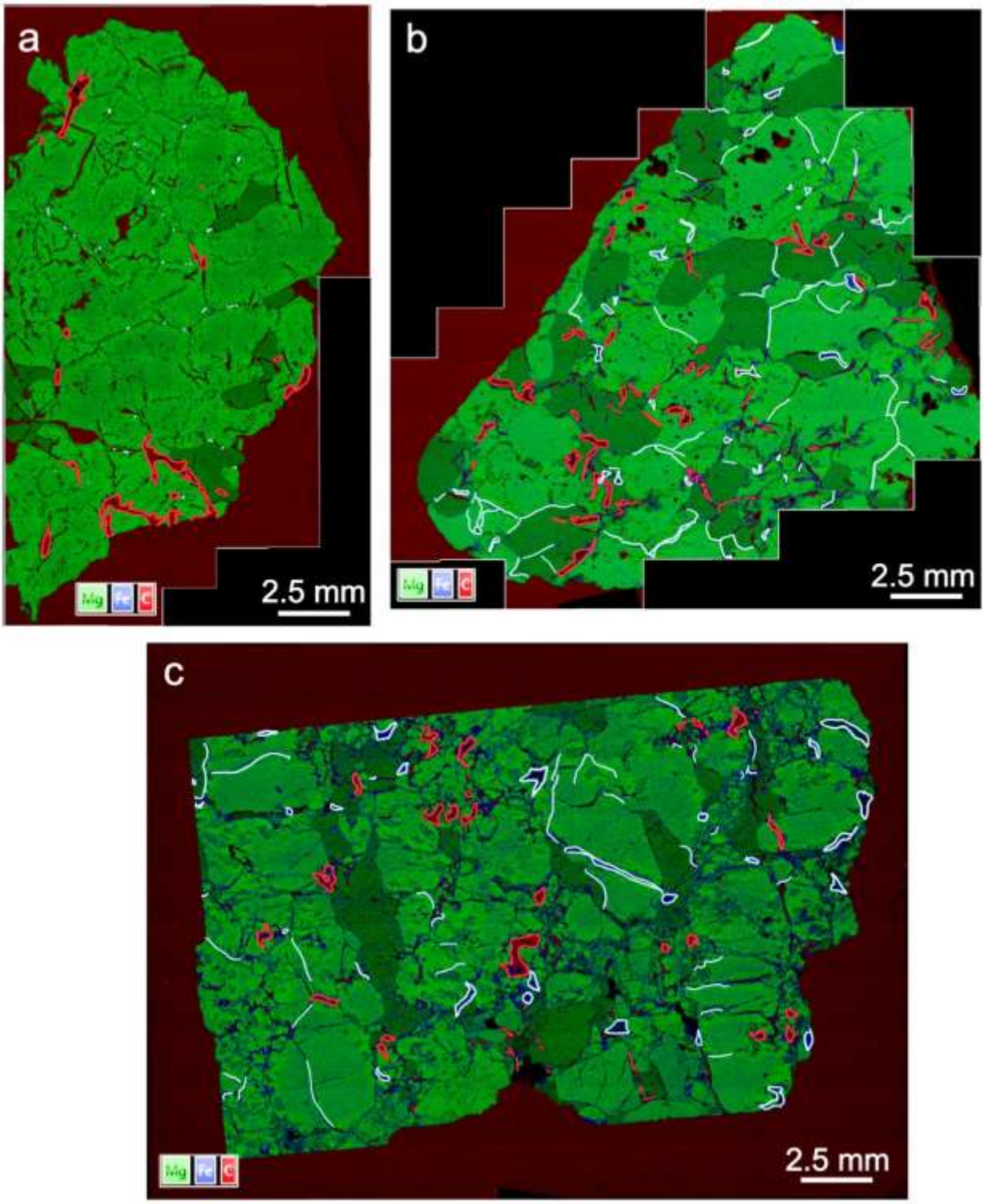

Figure 28: False colour EDS layered montage electron image of the bulk composition of ureilites samples (Red: carbon; Blue: iron; Green: magnesium) demonstrating the major abundance of iron-rich metal (light blue lines) and carbon (outlined in red) relative to the composition each of the samples. (a) Within the Haverö sample, carbon is visible across the sample but is predominantly concentrated in the lower half of the sample section iron-rich metal blebs are distributed across the whole section. (b) Nova 001 sample shows iron-rich metal veins and carbon regions spread across the entire sample. (c) Reid 016 shows a spread of carbon regions and iron-rich metal veins across the whole sample.

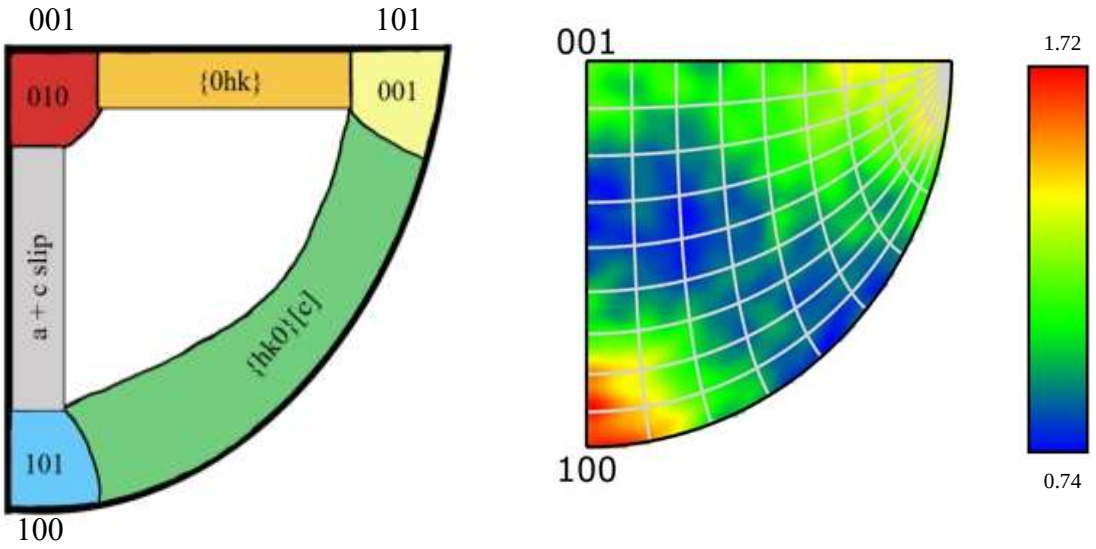

Figure 29: Slip system crystal rotation axis (CRA) diagram of olivine in Reid 016 (right) compared to Ruzicka and Hugo, 2018 (left) in the CRA plot of Ruzicka and Hugo, (2018) the colours represent implied deformation temperatures becoming progressively warmer from blue to green, yellow, orange and red. The grey area represents a special case, where the slip system is not directly related to deformation temperature. CRA-diagram of Reid 016 (right) showing the rotation axis accommodating pixel-pixel misorientation, showing a strong data cluster around the <100> axis and a fainter cluster around <010> that relate to cooler and moderate deformation temperatures respectively (Ruzicka and Hugo, 2018).

4.2 Anomalous Achondrite

MIL 090356 and its associated pairs (MIL 090340, MIL 090206, MIL 090895, MIL 090963 and MIL 090405) were originally classed as ureilites due to the olivine grains having carbon-rich rims containing metal and the composition of the cores of olivine and pyroxene grains (Goodrich et al., 2017), before being reclassified as ungrouped primitive achondrites due to high ferrous olivine compared to ureilites (Goodrich et al., 2017). MIL 090356 was classed as being brachinite-like based on a high coarse olivine content containing triple junctions (Keil, 2013). As such, it would be expected that MIL 090356 to show petrological and textural similarities to both ureilites and brachinites.

MIL 090356 is composed of coarse-grained olivine (60 area%) and pyroxene (3 area%) with olivine crystals that meet at 120° triple junctions. This texture is exhibited by both ureilites and brachinites (Keil, 2013). The olivine in MIL 090356 has a high Fo content of 71% and

iron veins that is similar to that seen in brachinites (Goodrich et al., 2017; Singletary et al., 2013; Keil, 2014).

MIL 090356 shows the veining of iron metal (Fig.24a) with an average thickness of 0.078 mm across the sample, interpreting this as the iron intergrowth texture described by Goodrich et al. (2017). There are two theories as to the origin of the iron intergrowths within the MIL 090356, the first is of methane gas infiltration and the second of a sulphur-rich gas infiltration (Goodrich et al., 2017).

The first theory of methane gas infiltration reaction is shown in the equation below with methane reacting with the olivine to produce iron intergrowth, magnesium-rich olivine, CO_2 gas and water.

$$4(FeMg)SiO_4 + CH_4 = 4Fe + 4MgSiO_3 + CO_2 + 2\,H_2O$$

The second theory suggests that a sulphur-rich gas infiltrated the rock resulting in sulphuration of the olivine and producing sulphide veins (Goodrich et al., 2017).

$$(FeMg)_2SiO_4 + S_{2(g)} \leftrightarrow 2MgSiO_3 + 2FeS + O_{2(g)}$$

The methane gas reaction would produce Fe metal that is consistent with the Fe metal veins observed across the sample. However, the abundance of water and CO_2 produced by this reaction can also produce other secondary phases such as carbonates and phyllosilicates by water-rock reactions involving the olivine. This is not observed in MIL 090356. The sulphur-rich gas reaction would produce a substantial number of sulphides in the sample. The wt% bulk composition of the sample reveals the sample contains 1.2 wt% sulphur and 0 wt% carbon. False colour images of MIL 090356 show the presence of carbon, however, the carbon coating of the sample can affect the spectrum. The bulk sulphur content and the lack of other water-rock reaction products suggest that infiltration by a sulphur-rich gas is likely to be the catalyst within the MIL 090356 sample. The source of sulphur within the parent body is unknown but given the similarities in texture between MIL090356 and the ureilites it is possible that an impact event from a sulphur-rich impactor may provide the source of the sulphur to drive this reaction. This would indicate that impactor injection of materials into olivine-rich primitive achondrites is a common process in the Solar System.

Brachinites are known to contain pyroxene-troilite intergrowths along olivine grains due to sulphuration reaction occurring post-crystallisation from an infiltrating sulphur gas (Zhang et al., 2022; Singerling et al., 2013). Ureilites containing reduction rims as a result of redox reactions. MIL 090356 experienced the second equation of sulphur infiltration reaction causing iron intergrowths based on the 1.2 wt% of sulphur calculated, the lack of sulphur observed in the iron metal veining during the study suggests two possible outcomes. 1) a more complex reaction history to account for the lack of FeS which sees both carbon and sulphur infiltration taking place or 2) the second reaction is the true process that occurred on the parent body. Overall, the presence of sulphur in the sample suggests option 1 containing a more complex reaction history on the parent body. The similarities in reactions across these three groups suggest that the ureilites, MIL090356 and brachinite meteorites may be on a spectrum of primitive achondrite meteorites that have similar textures but are altered based on the composition of impactors. This method is a common pathway for reactions across primitive achondrites, suggesting a spectrum of planetary bodies which are similar, and MIL 090356 being a halfway house between ureilites and brachinites.

4.3 Aubrite

The current model for aubrite meteorites is that they are closely affiliated with enstatite chondrites where the aubrites are the product of differentiation from an enstatite chondrite precursor (Weisberg et al., 2006). Both aubrites and enstatite chondrites formed within the same >1 AU due to the highly reducing nature of the material they contain (Keil, 2010). However, aubrites are breccias and contain fragments of both ordinary chondrites and forsterite chondrites (Lipschutz et al., 1998; Rubin, 2010). This suggests a degree of mixing of inner Solar System material that impacted the aubrite parent body with ordinary and forsterite chondrite asteroids (Lipschutz et al., 1998; Rubin, 2010). However, to date, no enstatite chondrite material has been described surprisingly as it should be the dominant material in this region of the Solar System (Keil, 2010).

The textures and microstructures of the Cumberland Falls aubrite display three different and distinct textures which are as follows; course breccia, fine breccia and chondritic clasts (Fig.17). All three sections have vertical and horizontal fracturing of the larger pyroxene

grains (Fig.21,23) and a sharp boundary is present between each of the sections (Fig.19) as described in the literature (Weisburg, 2006; Binns, 1969).

The overall area % bulk composition for the achondrite material of Cumberland Falls it is predominantly pyroxene (83.8%) with minor amounts of olivine (7.4%), iron (3.5%), carbon (3.4%) chondrite material (1.9%) present.

The Mg# data collected on the Cumberland Falls sample produced an Mg# of 1.0. The Mg# of ordinary chondrites is between 0.01 to 0.9, while the Mg# of forsterite chondrites is 0.89. neither value matches the Mg# measured in the chondrite material in Cumberland Falls indicating it represents a new type of chondrite clast in aubrites. The enstatite chondrites (EL/EH) have an average Mg# of 1.0 (Wasson, 1971; Lipschutz et al., 1998; Goodrich and Delaney, 2000). The similarity between the Mg# of the Cumberland Falls chondrite clasts and enstatite chondrites suggests that the chondritic material included in the sample is of enstatite chondrite origin (Mg# 1.0).

The addition of enstatite chondritic material as clasts in aubrite meteorites is expected as they are believed to be linked. However, identifying that enstatite chondrites are present indicates that fragments were still present in this region of the Solar System bombarding the surface of the aubrite parent body.

Enstatite, ordinary and forsterite chondrite inclusions have now all been described in aubrites. Each accreted in a different region of the inner Solar System. Observing that they are all present as clasts in aubrites indicates efficient mixing of material in the inner Solar System. However, the Late Veneer and Grand Tack predict an influx of volatile-rich material from the outer Solar System into the inner Solar System (Albarède, 2009). This would anticipate that aubrite breccias may also contain carbonaceous chondrite clasts. To date such carbonaceous chondrite clasts have not yet been observed with aubrites. A systematic search should be undertaken for carbonaceous chondrite-like material in the aubrite meteorite record. If no carbonaceous chondrite material is present, it would imply that while inner Solar System mixing was present during the formation of the aubrite parent body it was effectively shielded from the late veneer of carbonaceous material.

4.4 Summary

The original aim of this study was to further understand the microstructures and petrology of the samples within this study. Throughout this thesis, the petrology and microstructures of all five samples have been studied and analysed to provide a deeper understanding of processes that occurred in different parts of the solar nebula.

The ureilites and anomalous achondrite have shown close similarities within their petrology and structures, with MIL 090356 also demonstrating links to brachinites as expected, with evidence of similar chemical reactions occurring across this region of space based on the impactor which collided with the planetary body. The aubrite sample provides a different story for a separate region of the early solar nebula, when combined with the literature provides evidence of the complete mixing of material within the inner 1 AU of the Solar System, but suggests a lack of mixing of material from the outer Solar System based on findings of this research and current literature.

The purpose of these findings is such that a deeper understanding of the regions within the Solar System can be understood in more detail. Consistent conditions occurring within the outer Solar System in which a series of chemical reactions occur based on the catalyst provided through an impactor occurred within more than one meteorite group. For the inner 1 AU region of the early Solar System, Cumberland Falls aubrite confirms the full mixing of chondritic and achondritic material within the inner Solar System.

5. Conclusions

This thesis has investigated the petrology and microstructures of achondrites meteorites bringing forward these conclusions:

For the ureilites, the abundance of iron and carbon forms a potential pattern, of high iron and low carbon content resulting in thicker reduction rims caused by redox reactions happening across the planetary body. This is observed within Reid 016 with the later recrystallisation of Haverö explaining for thicker rims to be produced compared to the iron/carbon content. Comparing iron and carbon content to reduction rim thickness of other ureilites can confirm

this. The redox reaction is caused by impact events producing low pressures of <10 MPa and temperatures of 1126 – 726 ºC (Wasson et al., 1976) in the ureilite's parent body history. Either multiple events across one or more UPB or a single event affected by the proximal-distal distances to the impact site. Accounting for differences in the amount of carbon injected into the system and the time period that the area was exposed to the correct temperature and pressures for the redox reaction to take place. Further study on correlations between the thickness of reduction rims and the amount of iron and carbon within ureilites as well as testing heterogeneous oxygen isotope shall help to provide a deeper insight into the extent of the redox reaction and nature of the impactors into the impact history of the UPB.

MIL 09036 the anomalous achondrite appears to be a missing link between the ureilites and brachinites sitting as a halfway house between these two groups. This suggests that there may be a spectrum of primitive achondrites altered by a range of impactors on their parent bodies in the early Solar System. If impact infiltration of material is driving redox reactions with carbon injection in ureilites and sulphur infiltration in MIL 090356 and brachinites, it suggests that this mechanism is common in primitive achondrites throughout the Solar System, while the type of reaction produced is dependent on the type of impactor that collided with the parent body. Addressing if there is a spectrum in which primitive achondrites sit, would be a systematic study of other primitive anomalous achondrites that can identify any other possible chemical reactions occurring within the primitive achondrite group plotting them between already existing major achondrite groups as part of this spectrum.

The aubrite shows that within the inner Solar System <1 AU, there is a large amount of mixing of inner Solar System chondritic material such as ordinary, forsterite and enstatite chondrites with the aubrite parent body. There is an absence of carbonaceous chondrite material identified in aubrites which is inconsistent with the late delivery of volatile-rich material by the late veneer, likely due to a small sample set of chondrite clasts. A systematic study of aubrites should be undertaken to try and find carbonaceous chondrite clasts to determine if the outer Solar System material did mix with the inner Solar System or not. Identifying if this material did mix will help define hypotheses such as the Late Veneer and Grand Tack that seek to explain how volatiles were introduced to planetary bodies such as Earth.

Reference List

Albarède. F (2009) Volatile accretion history of the terrestrial planets and dynamic implications. Nature 461, pp. 1227-1233.

Barrat, J.A., Sansjofre, P., Yamaguchi, A., Greenwood, R.C. and Gillet, P., 2017. Carbon isotopic variation in ureilites: Evidence for an early, volatile-rich Inner Solar System. Earth and Planetary Science Letters, 478, pp.143-149.

Berkley, J.L., Taylor, G.J., Keil, K., Harlow, G.E. and Prinz, M., 1980. The nature and origin of ureilites. Geochimica et Cosmochimica Acta, 44(10), pp.1579-1597.

Bevan, A.W., 2007. Early Solar System Materials, Processes, and Chronol
ogy. Developments in Precambrian Geology, 15, pp.31-59.

Bevan, A. (1996) 'Meteorites recovered from Australia', Journal of the Royal Society of Western Australia, 79, pp. 33.

Binns, R. (1969) 'A chondritic inclusion of unique type in the Cumberland Falls meteorite', Meteorite research: Springer, pp. 696-704.

Bland, P. A., Zolensky, M. E., Benedix, G. K. and Sephton, M. A. (2006) 'Weathering of Chrondritic Meteorites', in Dante. S, L. and McSween, H.Y. (eds.) Meteorites and the Early Solar System II: the University of Arizona Press, pp. 853-868.

Chambers, J.E. and Wetherill, G.W., 2001. Planets in the asteroid belt. Meteoritics & Planetary Science, 36(3), pp.381-399.

Ciesla, F. J., Davison, T. M., Collins, G. S. and O'Brien, D. P. (2013) 'Thermal consequences of impacts in the early solar system', Meteoritics & Planetary Science, 48(12), pp. 2559-2576.

Cumming, G. L. (1969) 'A recalculation of the age of the solar system', Canadian Journal of Earth Sciences 6(4), pp. 719-735.

Day, J.M., Corder, C.A., Cartigny, P., Steele, A., Assayag, N., Rumble III, D. and Taylor, L.A., 2017. A carbon-rich region in Miller Range 091004 and implications for ureilite petrogenesis. Geochimica et Cosmochimica Acta, 198, pp.379-395.

Dodd, R. (1981) Meteorites: A petrologic-chemical synthesis. Cambridge Press Syndicate of the University of Cambridge, p. 328.

Downes, H., Mittlefehldt, D. W., Kita, N. T. and Valley, J. W. (2008) 'Evidence from polymict ureilite meteorites for a disrupted and re-accreted single ureilite parent asteroid gardened by several distinct impactors', Geochimica et Cosmochimica Acta, 72(19), pp. 4825-4844.

Egerton, R. F. (2005) Physical principles of electron microscopy: An introduction in TEM, SEM and AEM. Springer

Gaffey, M.J. and Kelley, M.S., 2004. Mineralogical variations among high albedo E-type asteroids: Implications for asteroid igneous processes. In Lunar and Planetary Science Conference (p. 1812).

Goldstein, J. I. (2003) Scanning electron microscopy and X-ray microanalysis. 3rd edn. New York: Springer Science.

Goldstein, J. I., Newbury, D. E., Michael, J. R., Ritchie, N. W. M., Scott, J. H. J. and Joy, D. C. (2018) Scanning Electron Microscopy and X-Ray Microanalysis. 4th edn. New York: Springer New York.

Goodrich, C. A. (1992) 'Ureilites: A critical review', Meteoritics, 27(4), pp. 327-352.

Goodrich, C. A. and Delaney, J. S. (2000) 'Fe/Mg-Fe/Mg relations of meteorites and primary heterogeneity of primitive achondrite parent bodies ', Geochimica et Cosmochimica Acta, 64(1), pp. 149-160.

Goodrich, C. A., Jones, J. H. and Berkley, J. L. (1987) 'Origin and evolution of the ureilite parent magmas: Multi-stage igneous activity on a large parent body', Geochimica et Cosmochimica Acta, 51(9), pp. 2255-2273.

Goodrich, C. A., Kita, N. T., Sutton, S. R., Wirick, S. and Gross, J. (2017) 'The Miller Range 090340 and 090206 meteorites: Identification of new brachinite-like achondrites with implications for the diversity and petrogenesis of the brachinite clan', Meteoritics & Planetary Science, 52(5), pp. 949-978.

Grady, M. and Wright, I. (2006) 'Types of Extraterrestrial Material Available for Study', in Laurette, D. and McSween, H. (eds.) Meteorites and the Early Solar System II: Vol. - -. - ed. Houston: The University of Arizona Press, pp. 3-19.

Grossman, J.N. (1998) 'The Meteoritical Bulletin, No. 82, 1998 July', Meteoritics & Planetary Science, 33(S4), pp. A221-A239.

Halfpenny, A., 2010. Some important practical issues for the collection and manipulation of Electron Backscatter Diffraction (EBSD) data from geological samples. Journal of the Virtual Explorer, 35, pp.1-18.

Hasegawa, H., Mikouchi, T., Yamaguchi, A., Yasutake, M., Greenwood, R. C. and Franchi, I. A. (2019) 'Petrological, petrofabric, and oxygen isotopic study of five ungrouped meteorites related to brachinites', Meteoritics & Planetary Science, 54(4), pp. 752-767.

Johansen, A., Jacquet, E., Cuzzi, J.N., Morbidelli, A. and Gounelle, M., 2015. New paradigms for asteroid formation. Asteroids IV, 47, pp.1-492.

Jull, A. J. T., Wlotzka, F. and Donahue, D. J. 'Terrestrial ages and petrologic description of Roosevelt County meteorites', In Lunar and Planetary Science Conference.

Keil, K., 2010. Enstatite achondrite meteorites (aubrites) and the histories of their asteroidal parent bodies. Geochemistry, 70(4), pp.295-317.

Keil, K. (1989) 'Enstatite meteorites and their parent bodies', Meteoritics, 24, pp. 195-208.

Keil, K. (2014) 'Brachinite meteorites: Partial melt residues from an FeO-rich asteroid', Geochemistry, 74(3), pp. 311-329.

Langendam, A. D., Tomkins, A. G., Evans, K. A., Wilson, N. C., Macrae, C. M., Stephen, N. R. and Torpy, A. (2021) 'CHOS gas/fluid-induced reduction in ureilites', Meteoritics & Planetary Science, 56(11), pp. 2062-2082.

Lipschutz, M. E., Verkouteren, R. M., Sears, D. W., Hasan, F. A., Prinz, M., Weisberg, M., Nehru, C. E., Delaney, J. S., Grossman, L. and Boily, M. (1988) 'Cumberland Falls chondritic inclusions: III. Consortium study of relationship to inclusions in Allan Hills 78113 aubrite', Geochimica et Cosmochimica Acta, 52(7), pp. 1835-1848.

Maitland, T. and Sitzman, S. (2006) 'Electron Backscatter Diffraction (EBSD) Technique and Materials Characterisation Examples ', in Zhou, W. and Wang, Z.L. (eds.) Scanning Microscopy for Nanotechnology: Techniques and Applications Springer

Mayeda, T.K. and Clayton, R.N., 1980. Oxygen isotopic compositions of aubrites and some unique meteorites. In Lunar and Planetary Science Conference Proceedings (Vol. 11, pp. 1145-1151).

McSween, H. (1987) Meteorites and their parent planets. United States of America: Press Syndicate of the University of Cambridge.

McSween, H. (1999) Meteorites and Their Parent Bodies 2nd edn. New York: Cambridge University Press.

Merrill, G. P. (1920) 'The Cumberland Falls, Whitley County, Kentucky, meteorite'. Meteorite bulletin 2012

Miyamoto, M., Takeda, H. and Toyoda, H. (1985) 'Cooling history of some Antarctic ureilites', Journal of Geophysical Research: Solid Earth, 90(S01), pp. 116-122.

Nabiei, F., Badro, J., Dennenwaldt, T., Oveisi, E., Cantoni, M., Hébert, C., El Goresy, A., Barrat, J.-A. and Gillet, P. (2018) 'A large planetary body inferred from diamond inclusions in a ureilite meteorite', Nature Communications, 9(1).

Nestola, F., Goodrich, C.A., Morana, M., Barbaro, A., Jakubek, R.S., Christ, O., Brenker, F.E., Domeneghetti, M.C., Dalconi, M.C., Alvaro, M. and Fioretti, A.M., 2020. Impact

shock origin of diamonds in ureilite meteorites. Proceedings of the National Academy of Sciences, 117(41), pp.25310-25318.

Neuvonen, K., Ohlson, B., Papunen, H., Häkli, T. and Ramdohr, P. (1972) 'The Haverö ureilite', Meteoritics, 7(4), pp. 514-531.

Newton, J., Franchi, I. A. and Pillinger, C. T. (2000) 'The oxygen-isotopic record in enstatite meteorites', Meteoritics & Planetary Science, 35(4), pp. 689-698.

Potts, P.J., Bowles, J.F., Reed, S.J. and Cave, R. eds., 1995. Microprobe techniques in the earth sciences (Vol. 6). Springer Science & Business Media.

Raymond, S.N., O'Brien, D.P., Morbidelli, A. and Kaib, N.A., 2009. Building the terrestrial planets: Constrained accretion in the inner Solar System. Icarus, 203(2), pp.644-662.

Reed, S. J. B. (2005) Electron Microprobe Analysis and Scanning Electron Microscopy in Geology. Cambridge Cambridge University Press, p. 161.

Rochette, P., Gattacceca, J., BOUROT-DENISE, M., Consolmagno, G., Folco, L., Kohout, T., Pesonen, L. and Sagnotti, L. (2009) 'Magnetic classification of stony meteorites: 3. Achondrites', Meteoritics & Planetary Science, 44(3), pp. 405-427.

Rollinson, H.R., 2009. Early Earth systems: a geochemical approach. John Wiley & Sons.

Rubin, A. E. (2006) 'Shock, post-shock annealing, and post-annealing shock in ureilites', Meteoritics & Planetary Science, 41(1), pp. 125-133.

Rubin, A. E. (2010) 'Impact melting in the Cumberland Falls and Mayo Belwa aubrites', Meteoritics & Planetary Science, 45(2), pp. 265-275.

Ruzicka, A. M. and Hugo, R. C. (2018) 'Electron backscatter diffraction (EBSD) study of seven heavily metamorphosed chondrites: Deformation systematics and variations in pre-shock temperature and post-shock annealing', Geochimica et Cosmochimica Acta, 234, pp. 115-147.

Savage, P. S. and Moynier, F. (2013) 'Silicon isotopic variation in enstatite meteorites: clues to their origin and Earth-forming material', Earth and Planetary Science Letters, 361, pp. 487-496.

Schaefer, L. and Elkins-Tanton, L. T. (2018) 'Magma oceans as a critical stage in the tectonic development of rocky planets', Philosophical Transactions of the Royal Society A: Mathematical, Physical and Engineering Sciences, 376(2132), pp. 20180109.

Schwarzer, R. A., Field, D. P., Adams, B. L., Kumar, M. and Schwartz, A. J. (2009) 'Present State of Electron Backscatter Diffraction and Prospective Developments', Electron Backscatter Diffraction in Materials Science: Springer US, pp. 1-20.

Singerling, S., McCoy, T. and Gardner-Vandy, K. (2013) 'Possible evidence for sulfidization reactions in the Miller Range brachinites'. Lunar and Planetary Science Conference, 1669.

Singletary, S. J. and Grove, T. L. (2003) 'Early petrologic processes on the ureilite parent body', Meteoritics & Planetary Science, 38(1), pp. 95-108.

Stöffler, D., Keil, K. and Edward R.D, S. (1991) 'Shock metamorphism of ordinary chondrites', Geochimica et Cosmochimica Acta, 55(12), pp. 3845-3867.

Stöffler. D, Hamann. C and K, M. (2018) 'Shock metamorphism of planetary silicate rocks and sediments: Proposal for an updated classification system', Meteoritics and Planetary Science, 53(1).

Swapp, S. (2017) Scanning Electron Microscopy (SEM). https://serc.carleton.edu/18401 (Accessed: 28 June 2022.

Tischer, F. (2018) The Grand Tack: An Overview of the Next Big Thing in Planetary Evolution. Bachelor, University of Graz.

Tomkins, A.G., Wilson, N.C., MacRae, C., Salek, A., Field, M.R., Brand, H.E., Langendam, A.D., Stephen, N.R., Torpy, A., Pintér, Z. and Jennings, L.A., 2022. Sequential Lonsdaleite to Diamond Formation in Ureilite Meteorites via In Situ Chemical Fluid/Vapor Deposition. *Proceedings of the National Academy of Sciences*, *119*(38), p.e2208814119.

Treiman, A. H. and Berkley, J. L. (1994) 'Igneous petrology of the new ureilites Nova 001 and Nullarbor 010', Meteoritics, 29(6), pp. 843-848.

Vdovykin, G. (1976) 'The Haverö meteorite', Space Science Reviews, 18(5-6), pp. 749-776.

Verkouteren, R. M. and Lipschutz, M. E. (1983) 'Cumberland Falls chondritic inclusions—II. Trace element contents of forsterite chondrites and meteorites of similar redox state', Geochimica et Cosmochimica Acta, 47(9), pp. 1625-1633.

Walker, D. and Grove, T. (1993) 'Ureilite smelting', Meteoritics, 28(5), pp. 629-636.

Wallis, D., Hansen, L. N., Britton, T. B. and Wilkinson, A. J. (2019) 'High-Angular Resolution Electron Backscatter Diffraction as a New Tool for Mapping Lattice Distortion in Geological Minerals', Journal of Geophysical Research: Solid Earth, 124(7), pp. 6337-6358.

Warren, P. H., Ulff-Møller, F., Huber, H. and Kallemeyn, G. W. (2006) 'Siderophile geochemistry of ureilites: a record of early stages of planetesimal core formation', Geochimica et Cosmochimica Acta, 70(8), pp. 2104-2126.

Wasson, J. T. (1985) Metorites: Thier record of early solar system history. United States of America: W.H. Freeman.

Wasson, J. T., Chou, C. L., Bild, R. W. and Baedecker, P. A. (1976) 'Classification of and elemental fractionation among ureilites', Geochimica et Cosmochimica Acta, 40(12), pp. 1449-1458.

Welisberg, M., McCoy, T. and Krot, A. (2006) 'Systematics and Evaluation of Meteorite Classification', in Laurette, D. and McSween, H. (eds.) Meteortites and the Early Solar System II. Huston: The University of Arizona, pp. 19-53.

Wlotzka, F. (1972) 'Haverö ureilite: Evidence for recrystallization and partial reduction', Meteoritics, 7(4), pp. 591-600.

Wlotzka, F. (1993) 'A weathering scale for the ordinary chondrites', Meteoritics, 28(3), pp. 460.

Wlotzka, F. (1993) 'The Meteoritical Bulletin, No. 74, 1993 March', Meteoritics, 28(1), pp. 146-153.

Zhang, L., Zhang, A.-C. and Wang, S.-Z. (2022) 'Apatite in brachinites: Insights into thermal history and halogen evolution', American Mineralogist In-press.DOI: 10.2138/am-2022-8712

Zhou, W., Apkarian, R., Wang, Z. L. and Joy, D. (2006) 'Fundamentals of Scanning Electron Microscopy (SEM)', in Zhou, W. and Wang, Z.L. (eds.) Scanning Microscopy for Nanotechnology: Techniques and Applications Springer